Simplification of Terahertz Spectroscopy Methods for Simultaneous Prediction of Density and Moisture Content in Wood

by

Sean L. Blackmore

B.Sc., University of British Columbia - Okanagan, 2018

THESIS SUBMITTED IN PARTIAL FULFILLMENT OF
THE REQUIREMENTS FOR THE DEGREE OF
MASTER OF SCIENCE
IN
PHYSICS

UNIVERSITY OF NORTHERN BRITISH COLUMBIA

May 2023

Abstract

For this thesis a new method for using terahertz spectroscopy to simultaneously measure density and moisture content in wood was tested for potential commercial use. Generally terahertz spectroscopy systems are nonviable for commercial applications due to the expense and complexity of most terahertz systems. However, simple and less expensive terahertz interferometer systems could be applicable if the phase and amplitude measurements of such a system could predict the density and moisture content just as well as other terahertz systems. As such, using a single frequency source in an interferometer configuration the phase and amplitude measurements are quantitatively evaluated to simultaneously predict density and moisture content. Medium density fiberboard is studied using the system and compared directly to terahertz time-domain spectroscopy measurements, demonstrating that both systems are able to achieve simultaneous prediction of density and moisture content. Therefore, it has been demonstrated that terahertz non-destructive evaluation of wood products, which requires expensive and complicated equipment, can also be performed using inexpensive single frequency sources and detectors suitable for use in industry today.

Table of Contents

List of Figures

List of Tables

1 Introduction

The Terahertz (THz) part of the electromagnetic spectrum is becoming highly useful for new technologies in both telecommunications and spectral imaging. Sometimes referred to as the "terahertz gap" due to the technology used to generate THz radiation is in it's infancy, new technologies and methods are in development to, for example, help alleviate the shrinking broadband space within the GHz bandwidth used by most wireless technology. Its advancement in telecommunications has been limited, however, due to the high absorption of THz radiation by water, limiting the range at which THz radiation can propagate. But this sensitivity to water is of use in the realm of spectral imaging. Its sub-mm wavelength and non-ionizing rays allows for clear images without the associated health risks as is the case with the more conventionally used X-rays, making it suitable for non-destructive evaluation (NDE). While THz radiation can not penetrate metals or water and can barely propagate past a few meters in the atmosphere due to absorption by atmospheric water vapors, many materials like wood and plastic are completely or nearly transparent when imaged using THz radiation [Federici, 2012], especially in the lower 0.1-2.5 THz range[Reid et al., 2013], which when combined with water's opacity allows for moisture to be detected within these materials. Moisture content (MC) in wood-based material is highly important to control to ensure structural stability, and because of its hygroscopic nature wood can very easily absorb or dissipate water vapor from or into the environment. This in turn will increase or decrease density as wood density is directly tied to moisture content [Inagaki et al., 2014], thus leading to studies into simultaneous measurements of the moisture content and density of wood samples necessary for implementing an industrial application of the method in the wood products industry.

2 Literature Review

2.1 History of THz Spectroscopy

2.1.1 Structural Studies

Traditional methods for measuring the attributes of wood samples, like density and MC, employ X-rays, near-infrared (NIR) waves and microwave radiation. Of these, microwaves produced the best results as the ionizing nature of X-rays is hazardous to living organic materials, especially to humans, limiting its use in an industrial setting, while NIR waves short wavelength lowered penetration, limiting its use to surface studies only [Jördens et al., 2010]. A number of experimental factors that must be accounted for, even in THz spectroscopy, were discovered in experiments conducted with microwaves. For example, measurements must be performed along the principle directions of the sample to prevent depolarization caused by the wood's grain to prevent errors in the measure-

ments [Bogosanovich et al., 2009]. Bogosanovich et al. observed major depolarization when receiving and transmitting antennas were cross-polarized, with the most occurring when the wood sample's grain was angled parallel to at least one antenna and the least when angled at 45° relative to both antennas. Meanwhile, when the antennas were co-polarized, transmission loss from depolarization was significantly less, especially when the wood sample's grain was angled perpendicular to both antenna's orientation. This was shown in their graphs seen in Figure 1, where the co-polarized set-up, designated HH for Horizontal-Horizontal orientation of the antennas, had less transmission loss relative to the cross-polarized set-up, labeled HV for Horizontal-Vertical orientation of the antennas, where transmission loss doubled even at 45°.

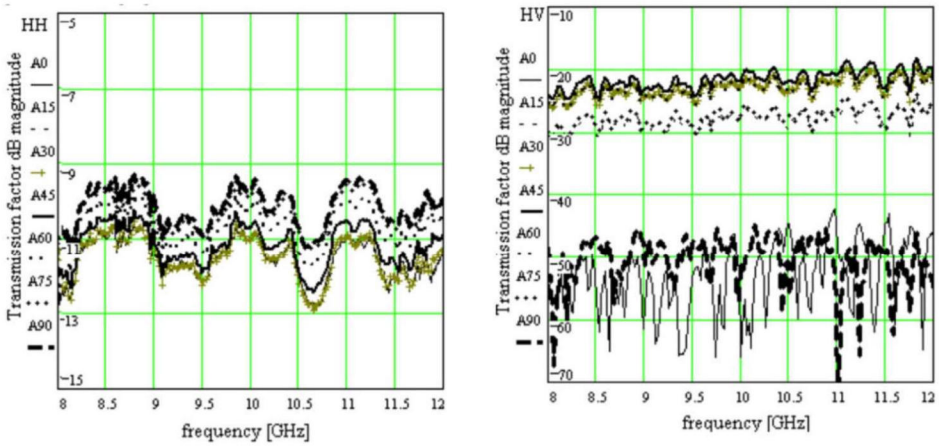

Figure 1: Co-Polarized vs Cross-Polarized antennas with horizontal left-side antenna from [Bogosanovich et al., 2009]. Each line represents a 15° angle step polarization of the sample based on the angle between the sample's grain and the left-side antenna. Similar results were also found with a vertical left-side antenna set-up

As such, THz spectroscopy tests are best performed with co-polarized transmitters and receivers and with the sample oriented perpendicularly to the antennas to reduce depolarization effects.

However, while microwaves penetrate samples unlike NIR waves, its longer wavelength limits spatial resolution [Jördens et al., 2010]. THz overcomes these limitations for wood, polymer and wood-polymer composite imaging as THz waves penetrate these materials like microwaves while having a shorter wavelength allowing for higher spatial resolution. In addition, unlike X-rays, low frequency THz radiation is non-destructive to organic samples since its radiation is non-ionizing, particularly in the 0.1-0.4 THz range, a range at which wood appears transparent in THz spectroscopy systems[Reid et al., 2013]. As well, X-rays are not sensitive to wood's fiber structure, preventing its use in monitoring systems[Reid et al., 2013]. In fact, experiments have shown that in the THz spectrum sample results have been shown to have unique signal responses based on the chemical composition of the sample. An example of this was shown in an experiment by Zhang

et al. who were, in conjunction with a feedforward neural network system called an Extreme Learning Machine, able to accurately identify agricultural pellets containing different dried herbs with near 100% accuracy [Zhang et al., 2018]. Most importantly, as THz frequencies are very sensitive to water in all its forms, including free and bound water that would be observed in wood/wood-polymer materials, THz technology may be an ideal candidate for water detection in wood. Studies have demonstrated success in measuring water content in similar materials, such as leaves [Hadjiloucas et al., 1999] and paper [Banerjee et al., 2008], [Mousavi et al., 2009].

2.1.2 Moisture Content Studies

In Hadjiloucas et. al's experiment, they were able to observe an increase in transmittance as the leaves underwent natural water loss, while a separate experiment observed loss in average leaf thickness relative to the cubic root of its natural water loss. This in turn shows a direct relation between moisture content and leaf thickness, which in turn would be related to the average leaf density. Meanwhile, Banerjee et al. were able to accurately quantify moisture content in paper. Their results showed a linear relation between moisture content and the phase shift of the THz signal transmitted through the paper, where an increase in phase shift related to an equivalent increase in moisture content. As well, the highest measured relative absorbance was only found to be a quarter of the dynamic range, meaning THz spectroscopy could handle four times the moisture content observed, 2.5 kg water/kg fiber, before the signal approached the noise floor. Thanks to THz's sub-mm wavelength, the micro-structure of the paper could be ignored and the samples treated as if they were a homogeneous medium. This was because the scattering caused by surface irregularities had minimal effect on the spatial resolution as the wavelength was significantly larger than material or surface irregularities [Banerjee et al., 2008].This simplifies their experiment, but unfortunately is not something that can be generally done with wood/wood-polymer material, as the micro-structure occurs at a scale comparable to THz wavelength, and as such wood/wood-polymer must be treated as a heterogeneous material. Lastly, the work by Mousavi et al. built upon the results of Banerjee and other's work to develop a "methodology to determine thickness and paper composition simultaneously" using terahertz time-domain spectroscopy (THz-TDS). This was done by employing a Bruggeman model to relate the terahertz transmission to the physical attributes of the paper samples by modeling the paper as a dielectric slab made of heterogeneous dry and water content. Using the dielectric permittivites of the dry content (ε_d) and wet content (ε_w) with sample volume fractions of v_d and v_w respectively, the Bruggeman model defined the effective permittivity of the paper as,

$$\varepsilon_p = \frac{1}{4}(\beta + \sqrt{\beta^2 + 8\varepsilon_d\varepsilon_w}) \tag{1}$$

where $\beta = (3v_d - 1)\varepsilon_d + (3v_w - 1)\varepsilon_w$. Defining ε_d by the type of paper used and ε_w with the frequency-dependent double Debye model outlined by Jepsen [Jepsen et al., 2007], ε_d could be determined using the measured ε_p results of the THz-TDS and known value of ε_w. This method has proven to be effective with more complex samples, like wood, though it requires additional modelling to account for the complex structure as detailed later.

2.2 Wood Structure and THz-TDS Methods

The microscopic structure of wood is determined by various anatomical elements, in particular the cell wall and vertical cells. Chemically, the wood cell walls are made of cellulose, hemicellulose, lignin and other extractives. These materials are arranged into a cylindrical-like structure surrounding an empty free space, commonly called the lumen. This combination of cell walls and lumen is the reason why wood needs to be treated as an anisotropic material. When water is retained in wood, the micro-structure becomes a mixture of cell walls, water and air. When water is present in wood it is held within the lumen as free water or bonded within the cellulose or hemicellulose via hydrogen bonding, and as such is referred to as bound water. When wood is dried, the free water is preferentially evaporated as the hydrogen bonds are hard to break, until it reaches what is called the fiber saturation point (FSP) where only bound water remains at lower moisture contents. Therefore, wood at or below this FSP is made up of air space with water randomly distributed on or within the walls defining the cylindrical elements.

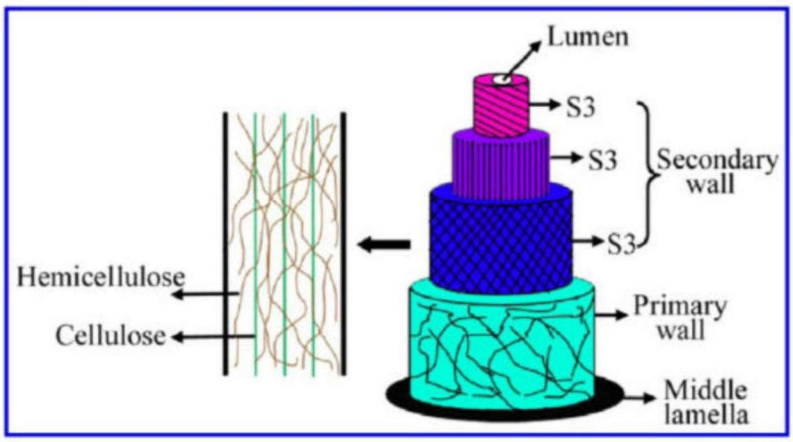

Figure 2: Wood cell structure from [Zhang et al., 2015]

An example of the wood cell structure can be seen in Figure 2, where the lumen is surrounded by 3 secondary walls made of lignin, cellulose and hemicellulose, and constitutes more than 80% of the cell wall thickness [Zhang et al., 2015]. Therefore, to properly measure the dielectric function from wood using THz spectroscopy, an Effective Medium Theory (EMT) must be used to account for the combination of water, air and

cell walls. Due to the structure of the wood, an assemblage called the composite cylinders assemblage (CCA), a 2D analogue of the composite sphere assemblage(CSA), has been used[Inagaki et al., 2014]. Originally developed by Z. Hashin, this model combines an outer concentric matrix shell with an inner circular fiber[Hashin, 1983], which can be used to describe the lumen between the cell walls and the boundary problem for the effective dielectric function of the material [Inagaki et al., 2014].

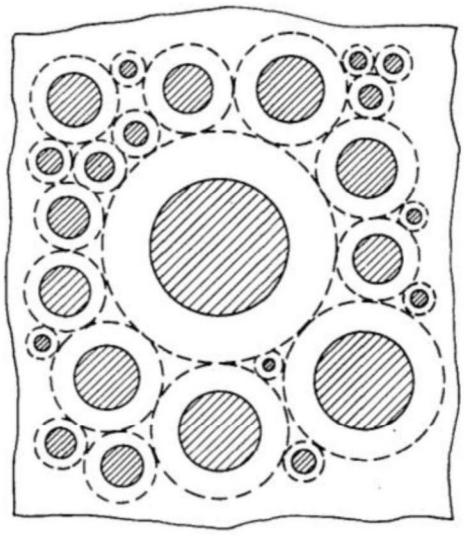

Figure 3: Composite Cylinder Assemblage (CCA) diagram from [Hashin, 1983]

In Figure 3 an example of a CCA is seen, where the outer shells of the cylinders represent the layers of secondary cell walls while the shaded inner fiber represent the lumen of the wood as detailed in Figure 2. The dielectric function obtained from THz spectroscopy of a sample is important, as the real and imaginary parts of the dielectric function have been shown to correlate with moisture content and density of wood samples, suggesting that simultaneous prediction of the moisture content and the density is possible[Inagaki et al., 2014]. The upper bound of the effective dielectric function can be obtained using the Maxwell-Garnet formula for infinite cylinders.

$$\frac{\varepsilon_{\text{eff}} - \varepsilon_{\text{h}}}{\varepsilon_{\text{eff}} + 2\varepsilon_{\text{h}}} = f_1 \frac{\varepsilon_1 - \varepsilon_{\text{h}}}{\varepsilon_1 + 2\varepsilon_{\text{h}}} \tag{2}$$

Here ε_{h} is the dielectric constant of the matrix shell and ε_1 is the dielectric constant of the inner circular fiber which is randomly distributed through the shell with a volume fraction of f_1 [Yang and Huang, 2007]. As this formula is asymmetrical, it can account for the possible randomness of the distribution and size of the tubes, though if cylindrical symmetry is known, a lower bound can also be found using the CCA model [Inagaki et al., 2014], and more rigorous knowledge of geometric models can help compute a solution for ε_{eff} that will be found to be between these bounds. This only accounts for the wood and

air portions of a wood sample, and another medium theory must be applied to account for the random distribution of the water within the cell walls. As mentioned before the Bruggeman model can be used define the effective permittivity of a sample that would be measured by a THz-TDS system. When combined with the Maxwell-Garnet model, these EMTs will describe the dielectric function of a wood sample and can be used to calculate the volume fractions of the air, cell wall and water within the sample so as to determine its density and moisture content.

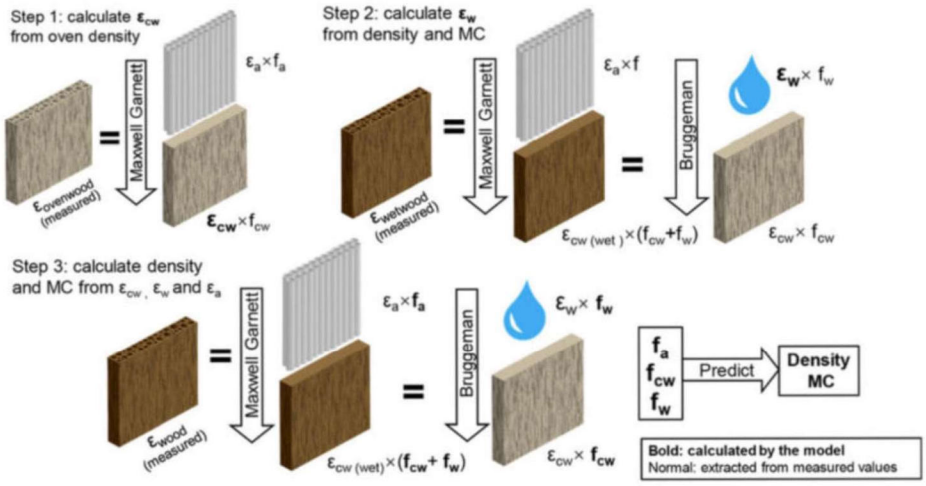

Figure 4: EMT Method for Density and Moisture Content Prediction by combining CCA and Bruggeman models from [Wang et al., 2019]

Figure 4 shows the step-by-step method to combine the separate models into an EMT that will define a standard wood sample. Originally the method employed by Inagaki et al. to predict density and moisture content could not account for a quadratic relation between the imaginary part of the dielectric function and the moisture content of the sample, thus predictions of the moisture content were either under or over estimated. However a more recent study by the same group in 2019 used the method in Figure 4 to more accurately predict the moisture content, albeit an issue of under/overestimation of the density and moisture content respectively with the only softwood type sample hemlock suggests a bio-structural difference that must also be accounted for [Wang et al., 2019].

As well as standard wood, it is important to be able to measure structured materials like particleboard and medium-density fiberboard (MDF) using similar models. This is due to fiberboards being a very common construction material with a wide range of uses and cheap production costs relative to standard wood. And while the chemistry of standard wood and structured material is the same, their structure is not. Both particleboard and MDF are made of residual wood fibers from both hardwood and softwood that is compressed into boards bonded by wax and resin. This means that cylindrical shape cannot be assumed as with standard wood, since the shape and orientation of the disparate

fibers will be far more randomized due to the compression. While this may seem like a disadvantage, it actually removes the polarization effect caused by the uniform direction of the wood grains, as seen in Bogosanovich et al.'s experiment. This is because the randomized, arbitrary distribution of the wood fibers will average their directions to approximately equal vertical and horizontal polarization. As well, MDF is generally manufactured at a moisture content of $8 \pm 3\%$, as a 1% change in moisture content results in a 0.35% change in thickness[European Panel Federation, 2015]. However, this value can be different and tighter depending on region of use, as it is common to manufacture MDF when the woods used are near their seasonal average moisture content for the region they will be used in[European Panel Federation, 2015].

3 Problem Statement

From previous experiments, measuring the dielectric function from THz time domain spectroscopy have given highly accurate results for measuring moisture content and density, however the equipment needed to perform this kind of test is complicated and expensive for use in industrial settings. For commercial use a piece of construction grade wood needs uniformity of both density and moisture content to meet strict guidelines set by safety regulations, as well as to properly produce many wood-based materials, like MDF where the moisture content needs be within 7-9% before applying resin for binding[Wilson, 2008] and overly dense materials would most likely correlate to reduced thickness[Domínguez-Robles et al., 2020]. As well, many construction materials are not purely of a uniform wood type, such as plywood and particleboard, so an EMT that can describe heterogeneous composite materials is needed. Thus, the method needs to be simplified to allow for equipment that can examine a larger sample quickly as it passes through a factory line, be able to handle different types of wood, and be less expensive. To meet these requirements, the simplest attributes that can by measured by a THz spectroscopy system are the phase shift and amplitude of a THz beam as it passes through a sample. And while high-end THz spectroscopy systems cannot be scaled for industrial use, other systems that can measure both the phase shift and amplitude of a THz spectroscopy system can be. Thus seeing if density and moisture content can be simultaneously predicted using only the phase shift and amplitude measured by a THz spectroscopy system will be the focus of this study.

4 Experimental Set-Up and Method

4.1 Sample Preparation and Data Acquisition Method

Wood samples are too complex for a viability test because of its anisotropic nature. Therefore, for this experiment three different thicknesses of commercial-grade MDF (Medium Density Fiberboard), 3/16", 1/2" and 3/4", were cut into several 75 mm x 75 mm squares to be used as samples. MDF was chosen for it's simplicity of structure relative to pure wood and higher water absorption potential, allowing for ease of measurement in a THz spectroscopy system. The samples were oven-dried overnight, removing both free and bound water from the samples and setting the MDF to 0% moisture content, then ordered by total oven-dry weight and split into groups of six (6) blocks where the samples were chosen to shrink the average mass of the group as much as possible. Five (5) of these groups were chosen to allow for the largest possible difference between these averages, to create the largest possible variance in the weight with such similar samples. One sample from each group was placed into one of six (6) desiccators, where each desiccator was prepared with different salts and/or amounts of water to prepare six different relative humidity environments. Because the samples within a group were as close in mass as possible, it would allow for better comparison between samples of similar dry mass but different moisture content. Thus, five samples of each thickness type would have a moisture content based on the desiccator, D1 to D6, they were placed in, resulting in a total of 90 distinct samples and a total of 180 volumetric measurements, counting both oven-dry and wetwood conditions.

Thickness Group	D1 - 11.3% RH	D2 - 78.2% RH	D3 - 91% RH	D4 - 31% RH	D5 - 65% RH	D6 - Water
3/16"	22.9-24.4 g	23.1-24.3 g	22.8-23.9 g	23.0-24.1 g	23.1-24.2 g	23.1-24.0 g
1/2"	52.5-53.2 g	52.2-53.3 g	52.0-52.9 g	52.4-53.5 g	52.6-53.4 g	52.0-53.0 g
3/4"	80.5-82.5 g	80.1-82.5 g	79.8-81.7 g	80.4-82.5 g	80.3-82.6 g	80.0-82.2 g

Table 1: Table of samples by desiccator. Range of mass represents range of oven-dry mass of samples in a group while RH stands for relative humidity of the desiccator.

These samples are tested in both the Picometrix system used for the 2014 Ingaki et al. and 2019 Wang et al. studies, and the new Terasense system so that a direct comparison can be made.

4.2 Measurement Method and Experimental Set-Up

4.2.1 Terasense System

Before full testing of the samples, the set-up needed testing to determine the best method to record the results. First, a new configuration that minimizes the footprint of the parts was prepared and tested relative to part configurations[Gehloff et al., 2020].

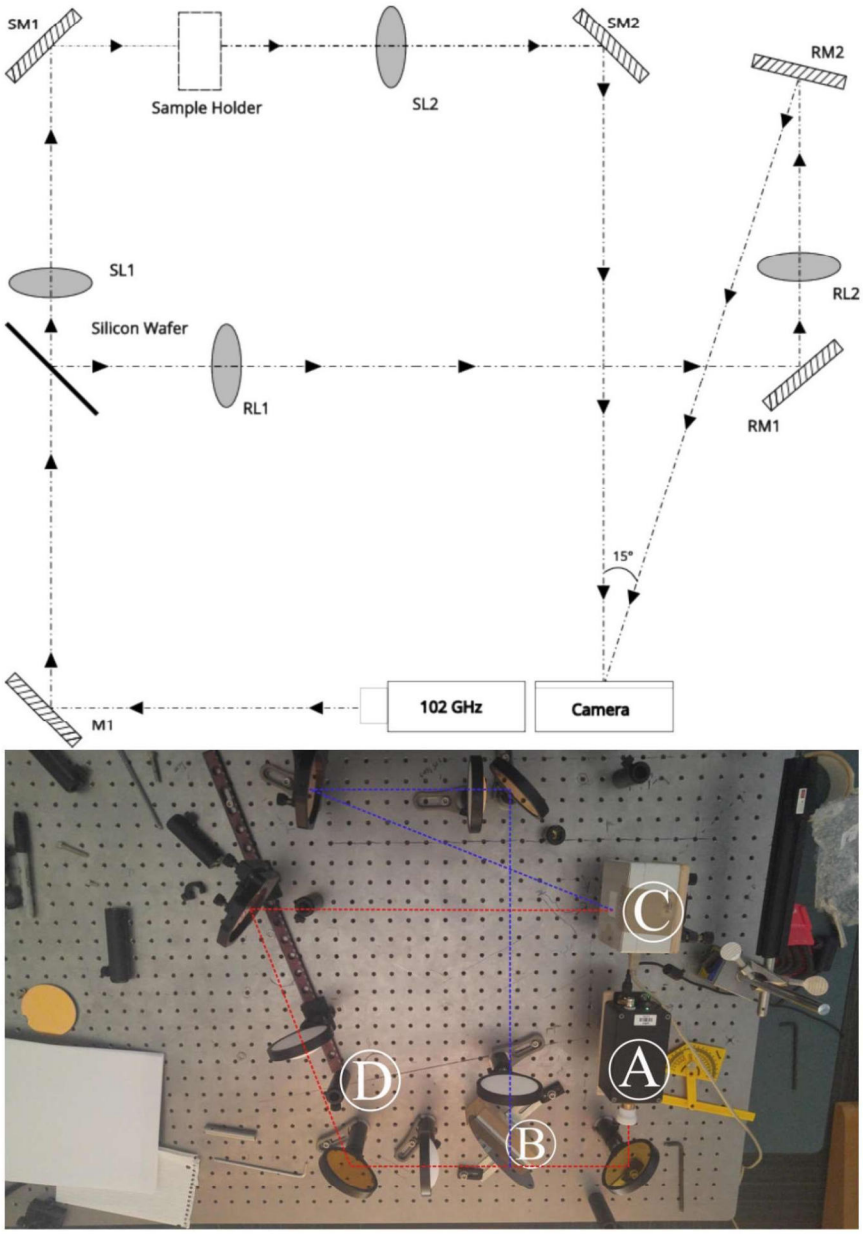

Figure 5: Diagram and top view of initial experimental set-up. Element A is the 102 GHz source, element B is the silicon wafer being used as a beam splitter, and element C is the camera and element D is where the sample holder is placed. The red line represents the transmission path while the blue line is the reflection path

This set up is a simple single pass Mach-Zender type interferometer which has the sample beam moving through the transmission path and with the reference beam along the reflection path before they recombine on the camera at an angle, as seen in Figure 5. The source used is a continuous wave (cw) source with a 60 mW output and a very narrow bandwidth created from a series of IMPATT diodes that averages around 102 GHz, while the camera is a Tera-256, a 16x16 pixel Terasense Terahertz Imaging Camera. A 102 GHz source was used because, as stated previously, wood is effectively transparent in

the low-frequency 0.1-0.4 THz bandwidth[Reid et al., 2013], and was the best available equipment for this experiment. As well, the wavelength of the the beams are $3mm$ in length, much longer than any surface roughness in the MDF that would effect the beams since MDF is both sanded and given a finish like wood veneer or lacquer, giving the MDF a roughness profile measured in μm instead of mm[Bal and Gündeş, 2020]. Along the paths, 3" optical lens with focal lengths of $115mm$ were used to colimate and focus the beams onto the camera to prevent both the beam spreading and diffraction rings occurring on the camera, as the source had a poor beam quality with an imperfect Gaussian profile and high M^2 value of 1.3[Price et al., 2020]. At first, testing was done at a 20° angle of interference, however later tests determined that a better fringe contrast with 2 fringes could be obtained around a 15° angle of interference. The 2 fringes were needed so that the separation between the primary fringe and a secondary fringe was distinguishable on the camera and so the fringes were wide enough to allow for fitting a predicted interference pattern to the measured interference pattern using the individual beam arm results. This will be described in more detail later, but to summarize a fitted interference pattern prediction is needed so that phase shift and amplitude of the sample can be measured. An example of the images produced by the Terasense camera, as well as an average linear response of these results, can be seen in Figure 6, where a 1/2" sample at 4% moisture content was used to produce the examples.

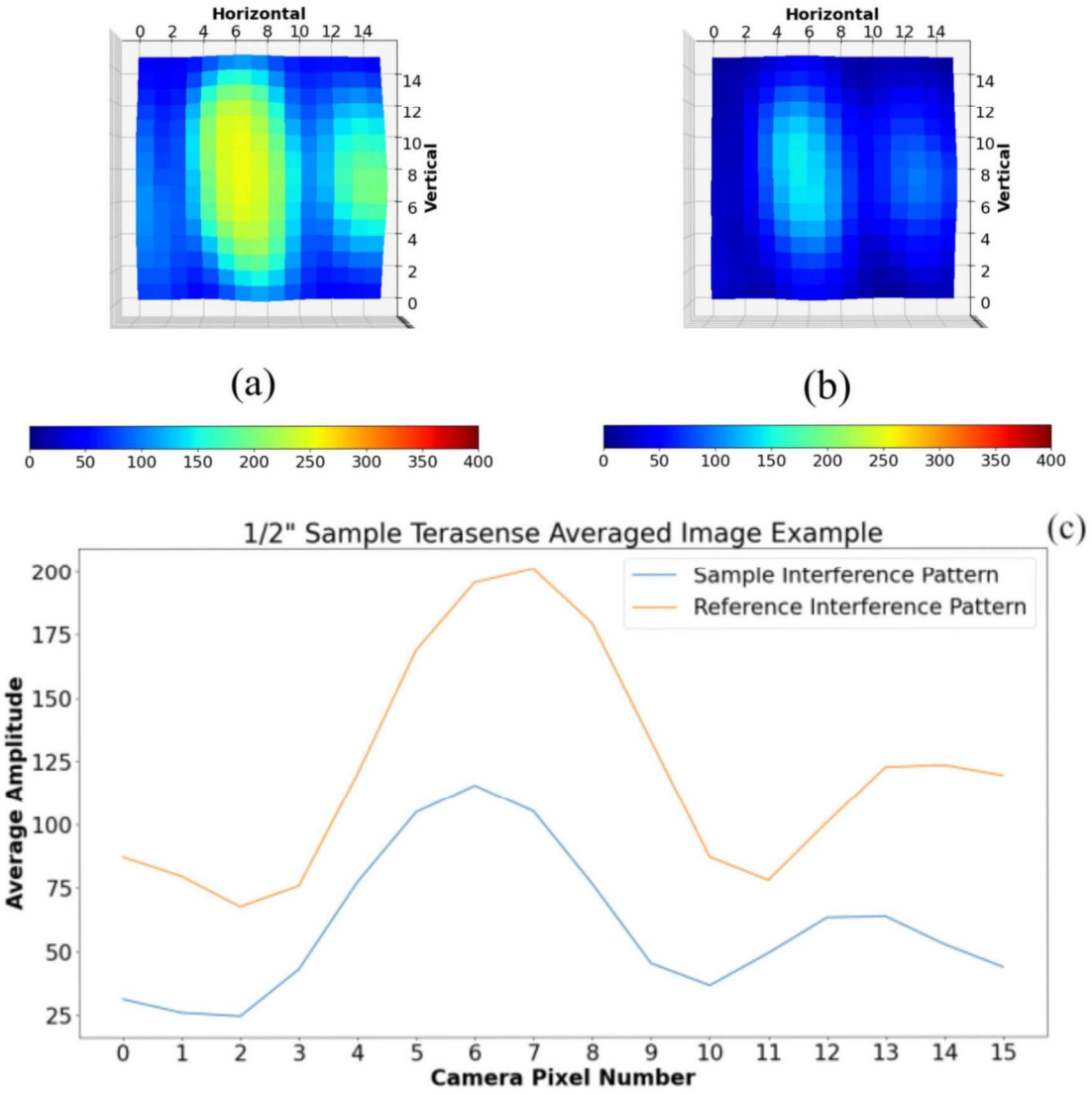

Figure 6: Examples of THz spectroscopy system output and averaged linear response. Figure 6a is an example of an interference pattern without a sample while figure 6b is an example of an interference pattern with a sample. Images from 6a and 6b are averaged into the linear response in figure 6c to be used for finding best-fit phase shift and amplitude values. Pixel numbers are used to better relate to camera images and because the unit dimensions are dependent on the angle of interference and wavelength of the source. All examples based on measurement of a single 1/2" sample with a moisture content of approximately 4%.

Figures 6a and 6b show an example of an interference pattern generated by the set-up with and without a sample in the system respectively, while Figure 6c are those images shows the averaged horizontal profile by averaging over the vertical dimension. Each pixel number represents one of the pixels of the Terasense camera along the horizontal, with a pixel size of 1.5 mm by 1.5 mm. Both the units of the x-axis and the amplitude value are dependent on the angle of interference of the split beams on the camera and the wavelength of the source, which will be detailed in Chapter 4.3. These interference patterns are used as a guide for the fitting algorithm used to determine the phase shift and amplitude values that will also be detailed in Chapter 4.3.

Initially, tests were conducted on paper, where the phase shift was measured as the number of papers placed in the sample arm was increased.

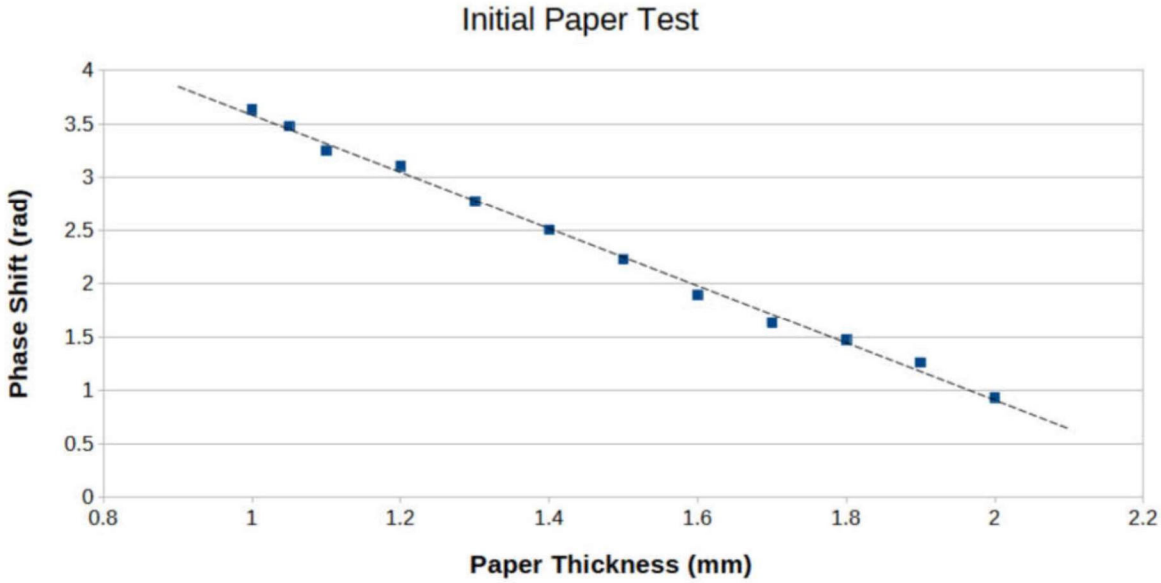

Figure 7: Linear relation between phase and thickness of paper sample

As seen in Figure 7, a clear linear relation between paper thickness and the phase shift is observed with the test results, in-line with the previously used experimental set-ups[Gehloff et al., 2020]. Only single measurements were taken as more paper was added to attenuate sample beam as this was simply a test to determine the functionally of the system and that the smaller set-up was consistent with past set-ups that used more space. The moisture content of the paper was 5-6%, based on the ambient humidity conditions of the lab and was measured under the same conditions.

For a more comprehensive test of the system to determine its accuracy and precision, a Ultra-High Molecular Weight polyethylene (UHMW) test was performed. The UHMW is a large wedge with a changing thickness along one of its faces, one ranging from 31.3 mm to 31.7 mm and the other ranging from 33.2 mm to 35.3 mm thick. Along the side of the wedge was a fixed ruler that could be attached to a sliding apparatus to measure

and shift the position of the wedge. The change in thickness was measured using the Terasense system and the resulting phase values could be varied with the thickness as was done in the paper tests. Measurements were taken three (3) times at distinct points along the length of the wedge to determine precision of the results. Position was shifted from thin to thick edge or vice-versa.

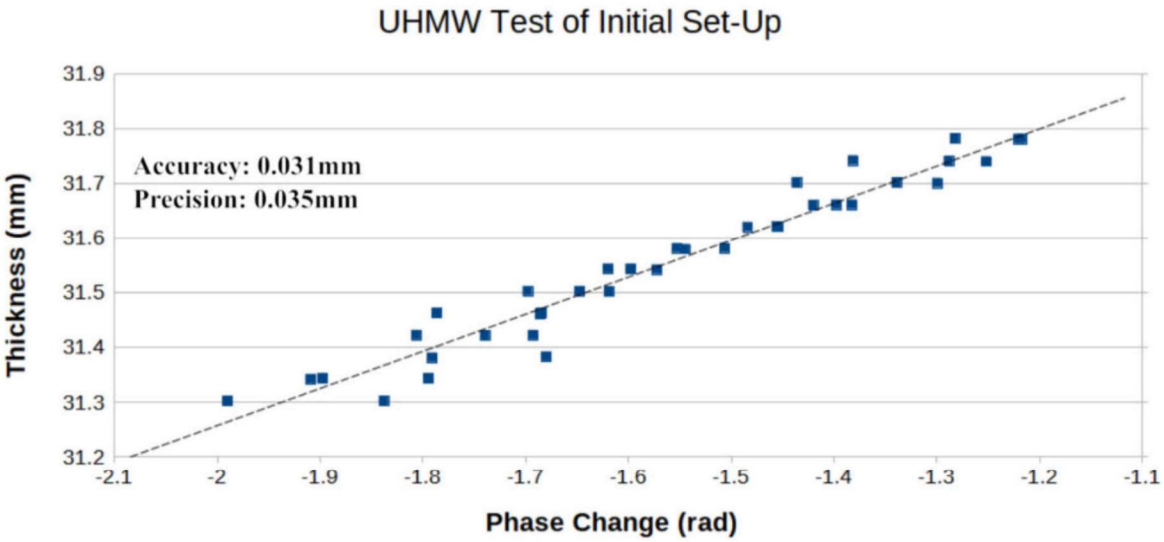

Figure 8: UHMW test results of initial experimental design. Precision determined by the average standard deviation of the measurements at the different points. Accuracy determined by average of the root mean square error (RMSE) of calculated thickness based on best fit line

Results found that the set-up had a precision of 35 μm, determined by the average standard deviation of the measurements at the different points along the wedge, and an accuracy of 31 μm, determined by the average Root Mean Square Error (RMSE) of the calculated values, which was inline with past UHMW tests results from older set-ups. The results of both the intial paper test and UHMW test confirm the viability of this experimental set-up for future testing.

During testing, it was discovered that results of predicted best-fit phase shift overestimated the amplitude of the response compared to the actual interference pattern. One possibility for this discrepancy is the coherence length of the signal being shorter than the path length difference of the arms of the interferometer. To test the coherence length of the 102 GHz cw Source, a Michelson interferometer was set-up.

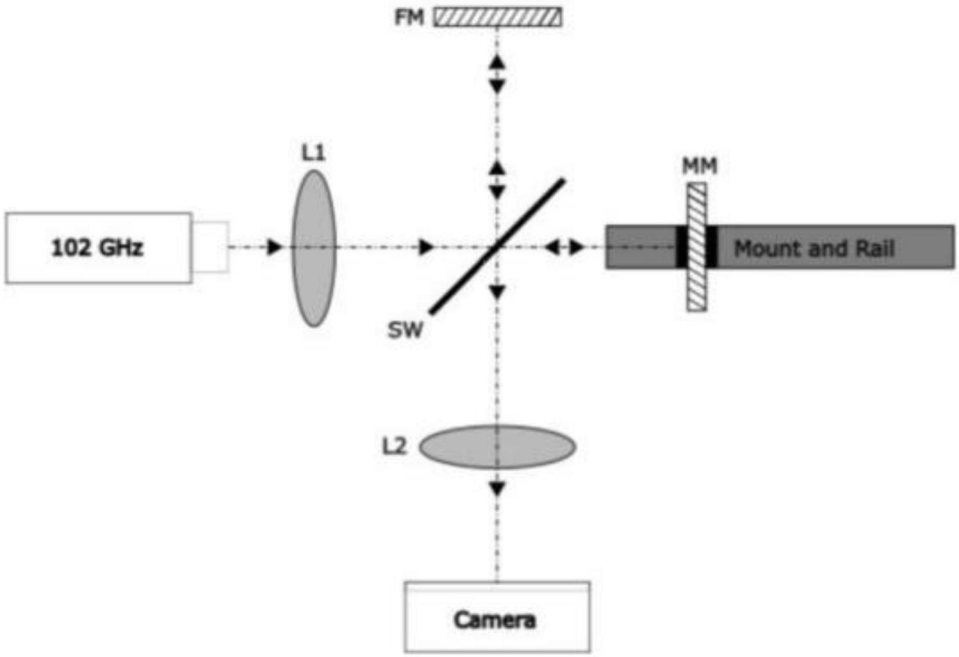

Figure 9: Diagram of Michelson interferometer used to test coherence length of source. L1 and L2 are lenses used to focus the source onto the camera. SW is a silicon wafer used as a beam splitter to split along the fixed and variable paths before recombining on the camera. FM and MM are mirrors, one fixed and the other mounted to a rail to allow changes to path length respectively.

Test results showed that the coherence length was over the maximum measured distance of up to 40 cm path length distance between the arms of the interferometer the fringe usually measured at. Reduced fringe visibility likely results from the diffraction limit of the source instead.

Another factor reducing fringe visibility is that the samples placed in the beam path reduced the intensity from 50/50 in the two arms. Generally, during testing of wood samples with the THz spectroscopy system, a silicon wafer was used as a beam splitter to create the reference and sample arm beams needed to recombine into an interference pattern on the camera. However, the silicon wafer creates even intensity beams between the arms, so a significantly thick and/or wet sample would attenuate the sample arm to a degree that only the reference arm's beam would appear on the camera. Normally, attenuating the reference arm to match the intensity of the sample arm would require using additional attenuation elements, like other samples, but this cannot be easily controlled and would require trial-and-error to find the right level of attenuation to equalize the beams of both arms. Instead, a variable beam splitter would allow for better control of beam strength between arms. This was made from a wiregrid polarizer acting as the beam splitter attached to a rotating apparatus used to adjust the angle of the wires of the polarizer. As the polarizer rotates, it is expected that the intensity of the beam will be unevenly split between the tow arms of the set-up relative to the angle of polarization,

with a perfect split expected to occur at relative 45° angles (i.e. 45°, 135°, 225°, 315°) and completely blocked in one or another arm at relative 90° angles (i.e. 0°, 90°, 180°, 270°). This allows us to reduce the intensity of the reference arm to match the intensity being received by the camera from the sample arm.

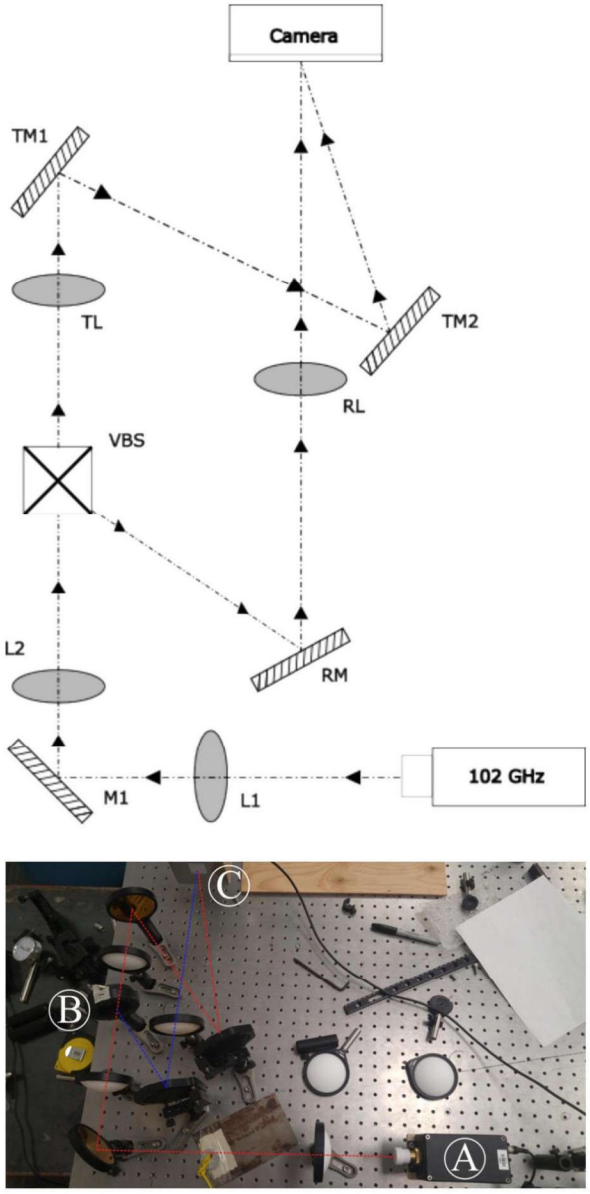

Figure 10: Variable beam splitter testing diagram and picture. L and M refer to lens and mirrors respectively, while T and R refer to the transmission arm and reflection arm paths respectively. VBS is the variable beam splitter used to split and control the signal strength along the separate arms. All elements in the top-down view are the same as with Figure 5, however element B is now the VBS

Figure 10 shows the experimental set-up used to test the polarizer as a variable beam splitter. This was done by measuring the intensity of the separate arms and the visibility of the fringe pattern as the angle of polarizer is varied. The results of this test can be seen in Figure 11, where the angle between the arms as they interfered on the camera was 18.9°.

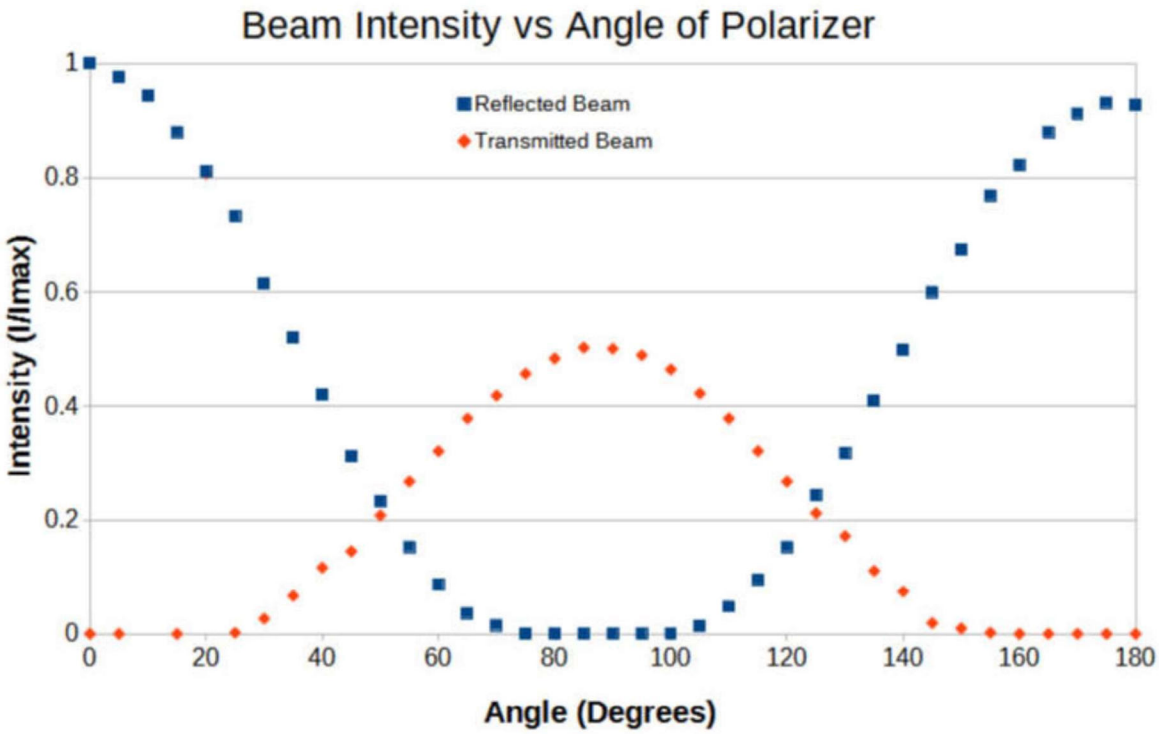

Figure 11: Variable beam splitter intensity vs angle comparison

As expected, the intensity of the two arms were nearly equal when the polarization angle was close to 45° and 135°, while at 0°, 90° and 180° one arm was completely blocked. Judging from the maximum intensity of the transmitted beam compared to the maximum reflected beam being half that of the reflected intensity is the likely reason the intensities are nearly equal at 50° and 125° instead of the expected 45° and 135°. The difference between the maximum intensity of the transmission and reflection arms is likely due to absorption of the transmitted beam by the polarizer, but this can be accounted for by erring on the side of the transmitted arm when using the polarizer in the final experimental set-up. This shows that the intensity of the beams can be controlled with this simple set up far more precisely than the previous method, and thus the polarizer acts as a superior substitute to the original silicon wafer.

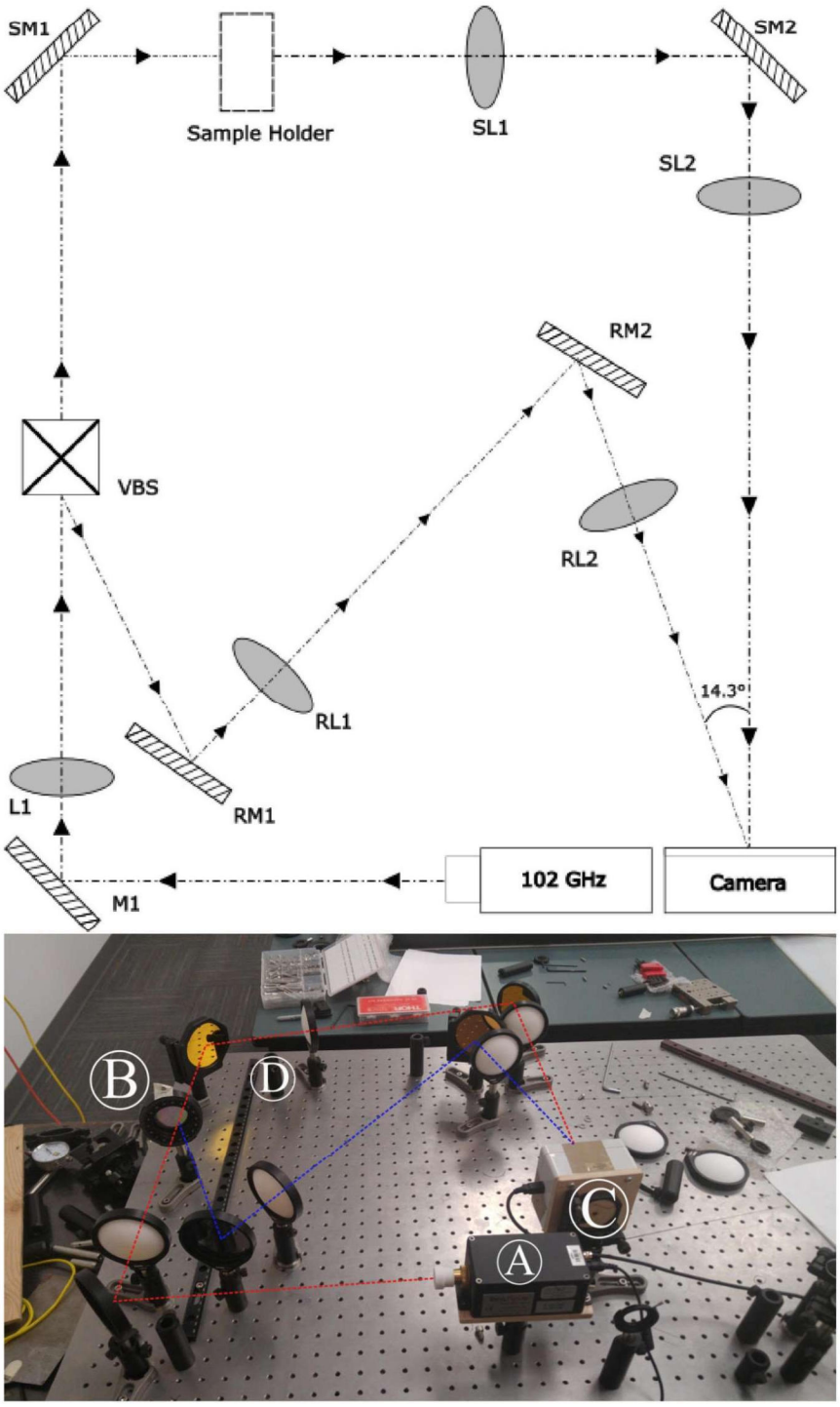

Figure 12: Diagram and picture of final experimental set-up. L and M refer to lens and mirrors respectively, while S and R refer to the sample arm and reference arm pathes respectively. VBS is the variable beam splitter used to split and control the signal strength along the separate arms. All elements of the top-down view are the same as with Figure 5, however element B is now the VBS.

The final set-up and design of the THz spectroscopy system can be seen in Figure 12. The sample holder used was a pair of parallel stands in which samples are placed, then mounted to a raised block to ensure the signal passed through the center of the samples. The final angle of interference chosen was 14.3°, based on results from the testing of the variable beam splitter. As mentioned in the last section, five different configurations of the system can be set to take a measurement of a sample. These are: an interference pattern of both arms with the sample, the sample arm with the sample, the reference arm, an interference pattern without the sample and the sample arm without the sample. These configurations relate to the results of the source on the camera as a metal sheet is used to block the beam of either arm as needed and whether the sample was placed in the system or not. To compare the precision of the system with the variable beam splitter to the system with the silicon wafer splitter, another test was done with UHMW.

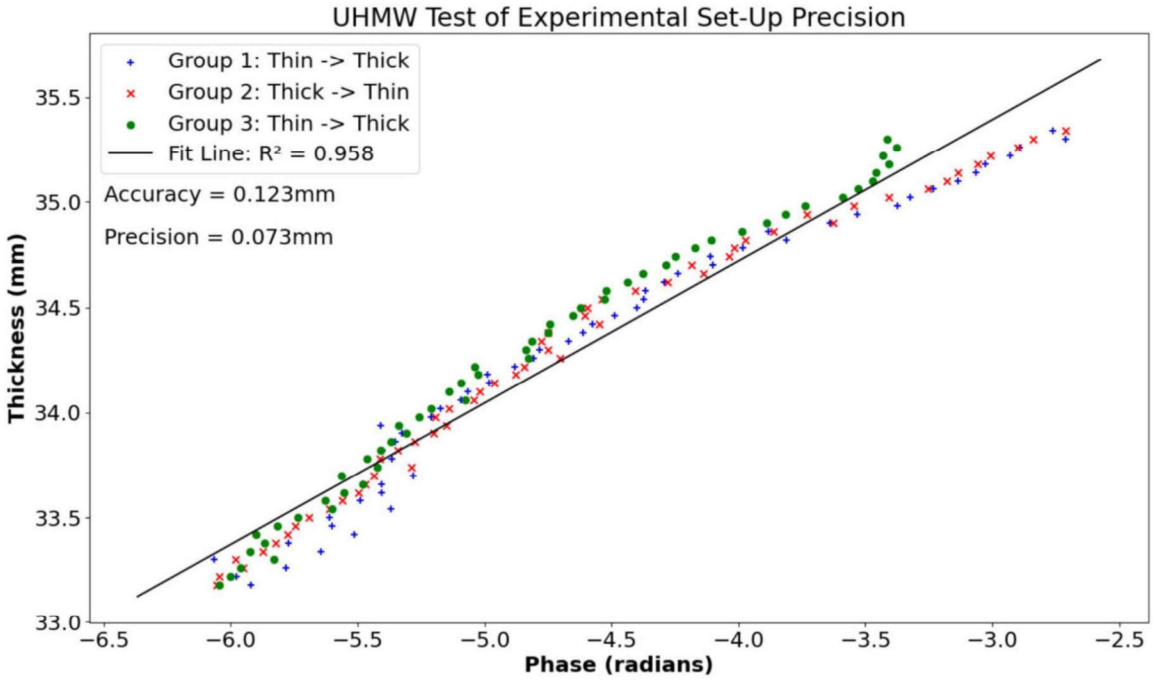

Figure 13: UHMW Experiment with VBS replacing silicon wafer. A reduction in the precision with a comparable UHMW test using a silicon wafer. Thick -> Thin and vice versa refer to direction UHMW was moved

The new set-up had a reduced precision of 73 μm from 35 μm and reduced accuracy of 123 μm from 31 μm, again based on the average standard deviation and average RMSE respectively. These results are likely caused by the general reduced total intensity from the variable beam splitter, but are still within an acceptable range relative to the difference in thickness of the samples.

For proper measurement of the samples, it was determined during that the best way

to collect data was to take five (5) measurements at different angular rotations of the sample at each of the five (5) different possible configurations of the system: interference pattern with the sample, interference pattern without the sample, sample path beam only with the sample, sample path beam only without the sample and reference path beam only. This was done by taking a measurement of the sample in each configuration, then rotating the sample 90° and taking the same 5 measurements, repeating for a total of 25 measurements of a single sample. All five configurations needed to be measured so that a predicted interference pattern could be generated using just the sample and reference arm to relate to the true interference pattern for phase extraction, and a reference interference pattern could be used as a base to determine the different absolute phase values and the change in amplitude. Five measurements of each of these configurations was done to provide an average of results as the position of the beam on the sample shifted slightly when the sample was rotated. Of note during testing it was noticed that the 102 GHz laser heated over time while active, leading to a heat-induced phase shift that could affect the results measured from the sample. A confirmation test of this phenomena was conducted by taking simple measurements of the phase value of a piece of paper every 20 minutes while the source remained on at all times. A noticeable change in the phase did occur during the test, however it was a sudden, discrete shift that occurred after nearly an hour of constant use, and was concurrent with a visually noticeable shift in amplitude on the camera during measurements. Therefore any shift caused by this could be accounted for since measured amplitude and phase changes were made in relation to the reference beam. Thus to compensate for this, after a sample was fully measured, the source was allowed to rest for approximately 10 mins between samples to reduce the chances of this heat-induced phase shift affecting results. And even if one were to occur, because the shift was both a discrete change instead of continuous and visually noticeable on the camera, so long as one didn't occur in the middle of a group measurements for one of the orientations of the sample then the phenomena could be ignored, as the phase shift and relative amplitude values are relative to the change between the sample interference and relative interference.

4.2.2 Picometrix System

Concurrently to the Terasense system, measurements were performed using a modified Picometrix T-Ray 4000 THz spectrometer. The T-Ray 4000 spectrometer generates THz measurements at a rate of 1000 waveforms per second in an 80 ps window having a bandwidth from 0.01-2.00 THz, according to manufacturer specifications, however usable bandwidth with samples in place is approximately 0.1-0.5 THz. We focus on the 0.1 THz frequencies for comparison to the Terasense experimental set-up. The THz beam diameter is taken as the $\frac{1}{e}$ electric field value that corresponds to the $\frac{1}{e^2}$ intensity value of the beam, which is colimated between the source and detector and has a value of 30mm at the

surface of the samples during measurements. Given the sample dimensions were 75mm x 75mm squares, the sampling effectively measures the average properties of the individual sample. For each MDF sample, THz transmission spectroscopy was performed and the time-domain waveforms of the transmitted THz radiation for each 90° orientation of the sample, further averaging the results over the full sample size. A pictorial representation consisting of a transmitter, receiver and a sample holder is given in Figure 14 below.

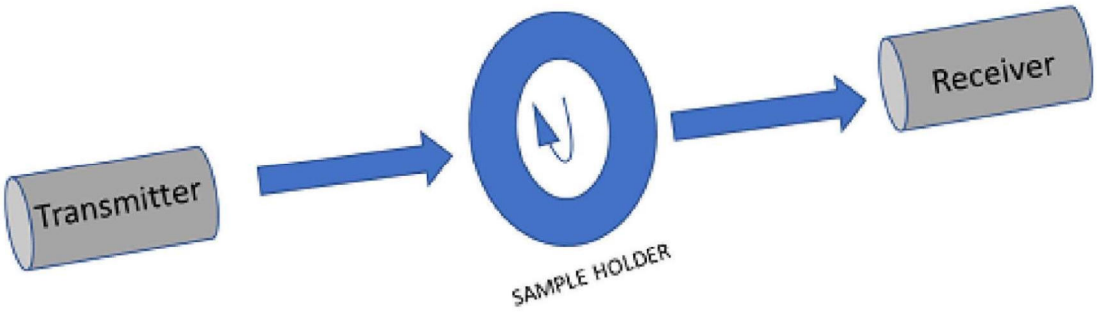

Figure 14: Diagram of Picometrix system

Prior to each transmission measurement, a reference measurement with an emptied sample holder was recorded. The transmitted and reference THz waveform was used to determine the complex index of refraction of the samples. An example of the signal response can be seen in Figure 15,

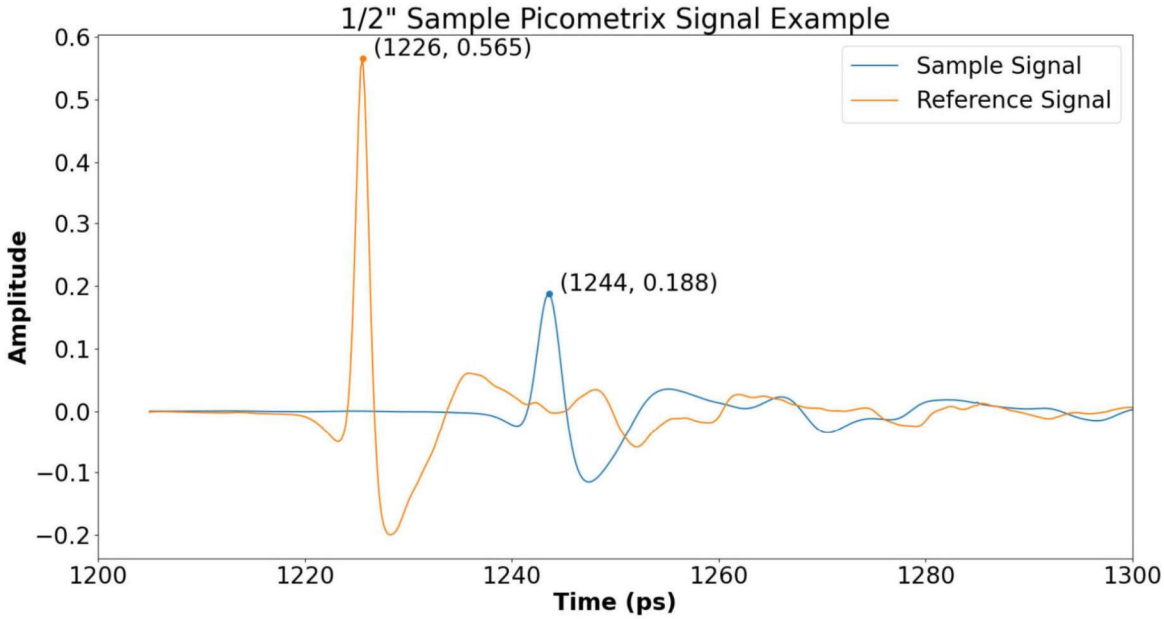

Figure 15: Example of Picometrix transmitted and reference signal response. Sample used to generate these signals is the same as was used for Figure 6. Points correspond to peaks of the respective signals

To compare Picometrix results to Terasense results, the time delay and relative amplitude values of the shifted transmitted/sample signal can be used. The relative amplitude is determined by taking the peak amplitude value of the sample and dividing it by the peak amplitude of the reference signal,

$$\alpha = \frac{\alpha_{sam}}{\alpha_{ref}} \tag{3}$$

The time delay, Δt, of the signal, which is the time difference between the peak signals, is directly related to the phase shift $\Delta\phi$ of the interference pattern,

$$\Delta\phi = \omega_f \Delta t \tag{4}$$

where ω_f is the angular frequency of the signal relative to its signal frequency,

$$\omega_f = 2\pi f \tag{5}$$

Equations (3) and (4) for the relative amplitude and phase shift are what is used to compare to the Terasense system results

4.3 Algorithms

4.3.1 Data Analysis

To extract the phase shift and amplitude values of the data received from the Terasense system, an algorithm is required to determine the best-fit values that recreate the measured interference pattern of the signal recombining from the sample and references arms of the experimental set-up. The equation for the intensity of a recombined beam is given by,

$$I(x) = I_1 + I_2 + 2\sqrt{I_1 I_2}cos(\delta), \tag{6}$$

where I_1 and I_2 are the intensities of the two beams and δ is the phase difference between the two beams. In the case where one of the beams is perpendicular relative to the camera, as in the experimental set-up, then δ varies across the camera. However the camera itself is made up of 16x16 pixel squares of a one (1) square inch optical lens. Therefore δ is defined as,

$$\delta(x) = x \cdot dx \cdot \theta \cdot \frac{2\pi}{\lambda} + \phi = \theta(x) + \phi, \tag{7}$$

where x is the horizontal pixel number, dx is the pixel width/spacing, θ is the angle between the reference beam and sample beam as the incident on the camera, λ is the wavelength in mm of the 102 GHz beam generator and ϕ is the absolute phase value of the interference pattern.

Of the two beams, the intensity of the reference arm will remain static while the intensity of the sample arm will change based on whether the sample has been inserted

into the apparatus or not. To determine what this change is the intensity of the sample beam can be defined as,

$$I_s = \alpha I_{refs}, \tag{8}$$

where I_s is the sample arm intensity with the sample, I_{refs} is the sample arm intensity without the sample and α is some value between 0 and 1 that reflects the attenuation of the sample arm by the sample.

If we insert equations (7) and (8) into (6) we get,

$$I_{inter} = I_{ref} + \alpha I_{refs} + 2\sqrt{\alpha I_{ref} I_{refs}} cos(\Theta(x) + \phi_s), \tag{9}$$

where $\Theta(x)$ is a 16x16 grid where each row is a sequential list of all $\theta(x)$ values as x ranges from 0 to 15, and by defining the reference interference pattern as,

$$I_{inter} = I_{ref} + I_{refs} + 2\sqrt{I_{ref} I_{refs}} cos(\Theta(x) + \phi_r), \tag{10}$$

then we can define the phase shift as $\Delta\phi = \phi_s - \phi_r$ or $\Delta\phi = \phi_r - \phi_s$, relative to whether $\phi_s > \phi_r$ or $\phi_r > \phi_s$ respectively. Thus by determining the best-fit values of α and ϕ_s for (9) and ϕ_r for (10) using the least squares method to fit a predicted interference pattern to the equations, we can determine the phase shift and amplitude values of the sample. As such, a Python script was implemented using this algorithm to analyze the data. As mentioned previously, samples were measured 5 times each to generate average amplitude and phase shift values for each sample from this algorithm with corresponding error bars.

4.3.2 Predictive Model

As stated in [Inagaki et al., 2014], the frequency-dependent transmission function $T(f)$ can be written in terms of the complex index of refraction of the wood samples derived from their dielectric function,

$$T_{wood}(\omega) = t_{as} t_{sa} e^{i2\pi f d(n_{wood}(\omega)-1)}, \tag{11}$$

where the index of wood n_{wood} is defined as the complex square root of the effective dielectric function, ε_{eff}, of the medium,

$$n_{wood}(\omega) = \sqrt{\varepsilon_{eff}(\omega)}, \tag{12}$$

f is the frequency of the signal, d is the thickness of the medium of transmission, or in this case the sample thickness, and t_{as} and t_{sa} are the Fresnel transmission coefficients at normal incidence of the transmission medium, into and out of the sample respectively, such that $t_{ij} = \frac{2n_j}{n_i+n_j}$ for the refractive indices n_i of the two media: air and the sample.

MDF is a combination of residual wood fibres bound together by wax and resin into boards. Since it is made from wood it shares the same cell wall structure and density as wood. When MDF is oven-dried it is made up of the cell walls and lumen of the cell wall structure, effectively meaning that the dielectric functions that affect a THz signal would be the dielectric functions of the wood cell walls and the air contained in the lumen. As well, the if we define the total fractional composition of MDF as the sum of all fractional components of the MDF, ie $1 = f_{cw} + f_a$, and define the effective dielectric function of MDF as the fractional sum of all dielectric functions affecting the signal, then using the known values of the dielectric functions of cell wall and air we can define the dielectric function of MDF. The dielectric functions of cellulose and air are measured in [Inagaki et al., 2014] as $\varepsilon_{\text{cw}} = 3.375 + i0.185$ and $\varepsilon_{\text{air}} = 1$ respectively, thus we can calculate the dielectric function of oven-dried MDF as,

$$\begin{aligned}
\varepsilon_{MDF}^{OD} &= \varepsilon_{cw} f_{cw} + \varepsilon_a f_a, \\
&= (3.375 + i0.185) f_{cw} + 1 * f_a, \\
&= (3.375 + i0.185) f_{cw} + 1 * (1 - f_{cw}), \\
&= (2.375 f_{cw} + 1) + i0.185 f_{cw},
\end{aligned} \tag{13}$$

where f_{cw} and f_a are the fractional composition of cell walls and air in the oven-dried MDF respectively.

To determine the f_{cw}, the geometry of the sample is used where we know that the density of the sample will be an equivalent composition of cell walls and air as seen in the dielectric function such that,

$$\rho_{MDF}^{OD} = \rho_a f_a + \rho_{cw} f_{cw} \Rightarrow f_{cw} = \frac{\rho_{MDF}^{OD} - \rho_a}{\rho_{cw} - \rho_a}, \tag{14}$$

and since $\rho_{MDF}^{OD},\ \rho_{cw} \gg \rho_a$,

$$f_{cw} \approx \frac{\rho_{MDF}^{OD}}{\rho_{cw}}, \tag{15}$$

The transmission function $T_{wood}(\omega)$ can be rewritten to split the real and imaginary parts of the index of the MDF as,

$$T_{wood}(\omega) = t_{as} t_{sa} \mathrm{e}^{i2\pi f d(n_R - 1)} \mathrm{e}^{-2\pi f d(n_I)}, \tag{16}$$

As previously found in [Inagaki et al., 2014], the real part of the dielectric function was tied to the phase shift/time delay of the Picometrix THz signals while the imaginary part was tied to the amplitude of the THz signals and we expect similar results from the Terasense system. As such we can define $T(\omega)$ in terms of ϕ and R as the phase shift and amplitude values respectively,

$$T(\omega) = t_{as}t_{sa}\mathrm{e}^{i\phi}R, \tag{17}$$

where $R = \mathrm{e}^{-2\pi f d(n_I)}$ and $\phi = 2\pi f d(n_R - 1)$

The effect the transmission function has on the signal can be written as,

$$E_{sam}(\omega) = T_{wood}(\omega)E_{ref}(\omega), \tag{18}$$

where the equations of the signal before and after moving through the sample are,

$$\begin{aligned} E_{ref}(\omega) &= E_0\mathrm{e}^{i2\pi(1)d}, \\ E_{sam}(\omega) &= E_0\mathrm{e}^{i2\pi n_{wood}(\omega)d}, \end{aligned} \tag{19}$$

Given that the normalized intensity of the signal measured in the Terasense system can be written as,

$$\frac{I(\omega)}{I_0} = \left(\frac{E_{sam}(\omega)}{E_{ref}(\omega)}\right)^2 = |T(\omega)|^2, \tag{20}$$

equations (17) and (20) can be combined to give,

$$\frac{I(\omega)}{I_0} = |T(\omega)|^2 = |t_{as}t_{sa}|^2 R^2, \tag{21}$$

If we assume $|t_{as}t_{sa}|^2 \approx 1$, which should hold true given $n_a = 1$ and $n_s \approx 1.4$, and we define A as the amplitude of the Terasense signal and ϕ as the phase shift of the signal, then by applying the substitutions from (16) into these parameters we get,

$$\begin{aligned} A &= R^2 = \mathrm{e}^{-4\pi f d n_I}, \\ \phi &= 2\pi f d(n_R - 1), \end{aligned} \tag{22}$$

where n_R and n_I can be defined in terms of (13),

$$\begin{aligned} n_R &= \sqrt{\frac{|\varepsilon_{MDF}^{OD}| + \varepsilon_R}{2}}, \\ n_I &= \sqrt{\frac{|\varepsilon_{MDF}^{OD}| - \varepsilon_R}{2}}, \end{aligned} \tag{23}$$

where ε_R is the real part of ε_{MDF}^{OD}. Of importance is the expectations with how the phase and amplitude values will change with regard to the index of refraction parts. From equa-

tion (22) we see that ϕ will have a linear relation with the real part given fixed frequency and thickness, while A will have an exponential relation with the imaginary part given fixed frequency and thickness.

For the wet samples we have to redefine the effective dielectric function to include the dielectric function of water. First we can define the dielectric function of the wet sample similar to that of the oven dried sample only now the fractional composition of the sample is defined as $1 = f_{cw} + f_a + f_w$,

$$\varepsilon_{MDF}^{WW} = \varepsilon_{cw} f_{cw} + \varepsilon_a f_a + \varepsilon_w f_w, \tag{24}$$

As was discussed in Chapter 2.1, the dielectric function of water is dependent on the frequency of the signal, and the equation is usually given using the double Debye model for frequencies around 1 THz as outlined in [Jepsen et al., 2007],

$$\varepsilon(\omega) = \frac{\varepsilon_s - \varepsilon_1}{1 - i\omega\tau_1} + \frac{\varepsilon_1 - \varepsilon_\infty}{1 - i\omega\tau_2} + \varepsilon_\infty, \tag{25}$$

where $\varepsilon_s = 73.36$, $\varepsilon_1 = 5.16$, $\varepsilon_\infty = 3.49$, $\tau_1 = 7.89ps$, $\tau_2 = 0.181ps$ and ω is again the angular frequency of the signal from equation (5), as defined in [Jepsen et al., 2007]. Solving equation (25) with ω given by the source frequency of 102 GHz, (25) can be simplified to,

$$\varepsilon_w = 7.58 + i13.18, \tag{26}$$

Inserting (26) into (24) and simplifying using the dielectric functions of the cell wall and air gives us the equation for the dielectric function of wet MDF, ε_{MDF}^{WW}:

$$\varepsilon_{MDF}^{WW} = 2.375 f_{cw} + 6.58 f_w + 1 + i(0.185 f_{cw} + 13.18 f_w), \tag{27}$$

To determine the fractional composition of water, f_w, we again use the geometry of the sample where the total density of the wet sample is the fractional composition of the density of all parts,

$$\rho_{MDF}^{WW} = \rho_a f_a + \rho_{cw} f_{cw} + \rho_w f_w, \tag{28}$$

While ρ_{MDF}^{WW} is an unmeasured value, it's value is dependent on the original oven dry density of the sample and the moisture content, MC, of the sample,

$$MC = \frac{\rho_{MDF}^{WW} - \rho_{MDF}^{OD}}{\rho_{MDF}^{OD}} \cdot 100\%, \Rightarrow \rho_{MDF}^{WW} = \rho_{MDF}^{OD}\left(\frac{MC}{100\%} + 1\right), \tag{29}$$

Inserting (29) into (28) and solving for f_w we get,

$$\begin{aligned} f_w &= \frac{\rho_a((1-f_{cw}))+\rho_{cw}f_{cw}}{\rho_w+\rho_a((\frac{MC}{100\%}+1)} \cdot \frac{MC}{100\%}, \\ &\approx \rho_{cw}f_{cw}\frac{MC}{100\%} = \rho_{MDF}^{OD} \cdot \frac{MC}{100\%}, \end{aligned} \tag{30}$$

Again, $\rho_{cw}, \rho_w \gg \rho_a$.

Using (27) in place of (13) in (23), we will get similar results for equation (22), only now more pronounced given water's larger affect on the dielectric function.

5 Results

As explained in Chapter 4.1, MDF samples were prepared to different moisture contents and measured using the Terasense phase-contrast and the Picometrix time-domain spectroscopy systems. During measurements of the samples in the Terasense system it was found that the 102 GHz source had difficulty penetrating the thicker samples at the higher moisture content levels due to absorption. The 1/2" samples could not be penetrated beyond 10% moisture content and the 3/4" samples could not be penetrated past 5% moisture content. As such, less data was collected using the Terasense system relative to the Picometrix system. Despite this limitation, results from the Terasense measurements have shown a high correlation between the amplitude and phase shift values measured and the known mass and moisture content of the conditioned samples, and produced results in reasonable agreement to the Picometrix THz measurements. As stated in Chapter 4.2.1, in the Terasense system each sample was measured 5 times in each of its 5 possible configurations, as the sample was rotated 90° after one complete group of the 5 configurations. For the results of simultaneous prediction to meet industrial standards, predictions for moisture content need to be within 2-3%[European Panel Federation, 2015], while predictions for density should be roughly $0.02 g/cm^3$[Theng et al., 2015], which is equivalent to variation in specific gravity of MDF from production methods[Eroğlu et al., 2001].

5.1 Dry Sample Results

5.1.1 Expected Dry Results

The dry samples were prepared by oven-drying the samples in a standard vacuum oven used for drying wood before being measured in the 2 systems. In the Terasense system the samples' amplitude and phase change values were measured and calculated as detailed in Chapters 4.1 and 4.3.1 respectively, allowing for comparisons of both measured phase and amplitude with variation of mass in the sample sets. For the dry samples it is expected that the phase change will exhibit an increasing linear relationship with increasing

mass, as the phase change is primarily dependent on the real part of the index of refraction of the samples, as expressed in equation (22). Inagaki et al. demonstrated an increasing linear relation between the real part of the index of refraction of the samples and the oven-dry density consistent with what is expected based on equation (22)[Inagaki et al., 2014]. Therefore, since the volumes of the samples are fixed within their thickness groupings, an increase in density is directly proportional to an increase in mass, thus an increase in phase change is directly proportional to an increase in mass. Meanwhile, the amplitude is expected to have an exponential relationship with the mass as amplitude is primarily dependent on the imaginary part of the index of refraction as seen in equation (22). This is to be expected because amplitude is proportional to the intensity of the signal from the analysis model in Chapter 4.3.1, and the use of normalized intensity is equivalent to transmittance as per equation (31), which is defined by the Beer-Lambert law as a decaying exponential function,

$$T = e^{-\tau d} \tag{31}$$

where d is the optical path length and τ is the absorbance of the attenuating material defined as,

$$\tau = \sigma n \tag{32}$$

where σ is the absorption cross section, and n is the number density of the attenuating species in cm^{-3}[Oshina and Spigulis, 2021]. Assuming σ is fixed given all samples are made of the same material, n is then proportional to mass density ρ_m by,

$$\rho_m = n\frac{M}{N_A} \tag{33}$$

where M is the molar mass of the sample in $\frac{g}{mol}$ and N_A is Avogadro's constant, then amplitude will suffer an exponential decay as mass increases. However, it should be noted that these assumptions are based on an absorption cross section σ that is constant across species, and any change in a sample's composition, for example a difference in resin content or wood chip distribution, would change the value of σ between samples.

In summary, we expect for dry MDF samples:

- Measured phase varies linearly with density/mass
- Measured relative amplitude varies exponentially with density/mass

5.1.2 Phase Results

As expected, linear relations between measured phase change and mass is evident in both the Terasense and Picometrix data sets. As detailed in Chapter 4.2.2, using equations (4) and (5) with the signal frequency of the Picometrix system, which measured the

samples over the 0.1-0.5 THz range, we can get the equivalent phase change value. For this experiment, using the 100 GHz portion of the range we can get a phase change value equivalent to the phase change generated by the 102 GHz source of the Terasense system.

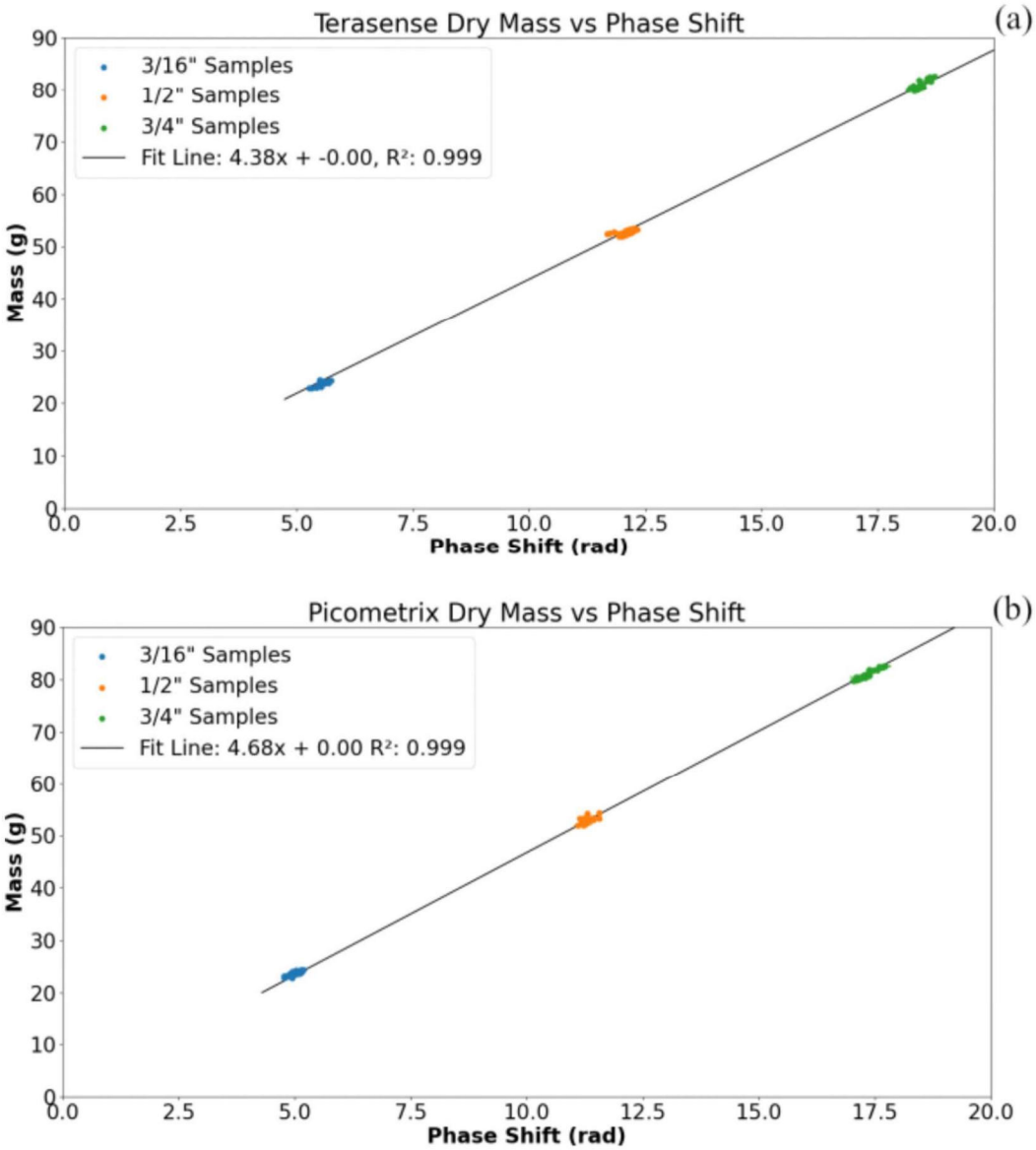

Figure 16: Mapping of dry mass varied with phase shift. Results show a strong linear relation with a minor difference in best-fit variable.

As seen in both Figures 16a and 16b, the least squares regression fitting line are roughly equal, meaning the systems are measuring equivalent results. The linear relation is expected on physical grounds, as a higher mass means more material the sample arm portion of the signal passes through before recombining with reference arm on the camera, therefore a longer time delay which directly relates to a larger phase shift.

5.1.3 Amplitude Results

As opposed to the exponential dependence of amplitude on mass that was expected, a large spread in amplitude values was observed within each thickness(mass) grouping. As well, a general trend of decreasing amplitude with increasing mass between sample sets was observed.

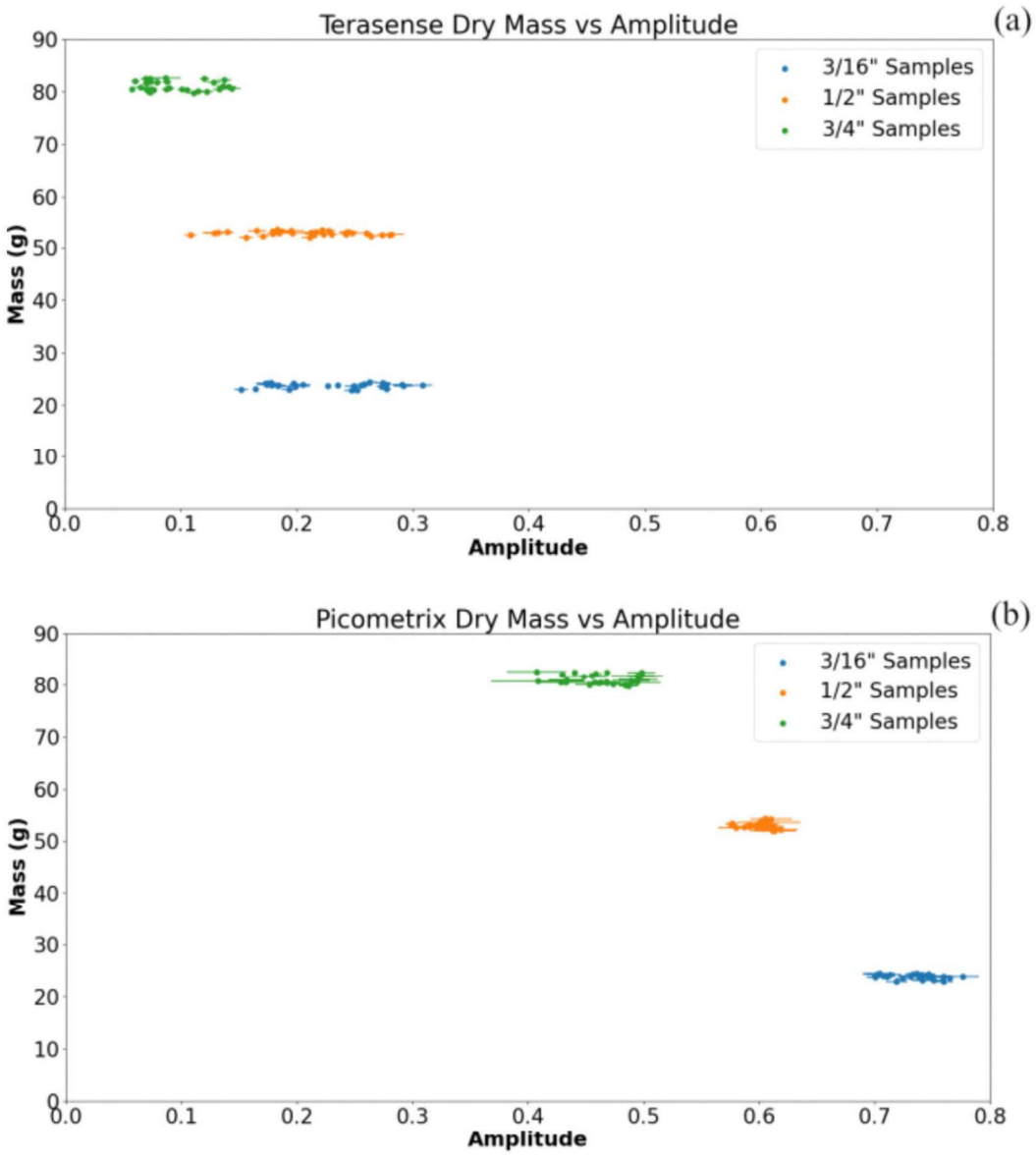

Figure 17: Mapping of dry mass to relative amplitude. Terasense and Picometrix data shows high variance of amplitude values with little variance in mass values instead of expected exponential decay. Higher amplitude value in Picometrix due to greater signal strength

As mentioned in Section 5.1.1, these results are likely from two factors that are un-

accounted for in simple Lambert-Beer's law exponential dependence. First is the fact that the MDF is not a homogeneous material but is instead a heterogeneous material made up of several wood chips of different sizes and species of wood, all held together with resin, generally Urea-Formaldehyde (UF) Resin. UF Resin in MDF typically varies between 8-12% by mass of total material in the board [Phanopolus, 2010], with the percentage in the samples varying by thickness as the manufacturing process is adjusted. Second is that when dealing with heterogeneous materials, the equation for absorbance is defined as the sum of the individual absorbance of the different species,

$$\tau = \sum_{i=1}^{N} \sigma_i n_i \tag{34}$$

If the simple equation for the Lambert-Beer's law held with a single absorption cross-section, then the low variance in the mass would be expected to exhibit a low variance in amplitude. Instead it is likely that the distribution in resin content and variation in species composition is producing a spread in amplitude values within each thickness grouping. In addition, scattering may contribute to the spread as the distribution of particle sizes may lead to a spread in amplitude values, and scattering cross-sections were not included. Further elucidating the nature of the spread is beyond the scope of this thesis work, as it did not form part of the prediction model that follows. As for the difference in amplitude values between the Terasense and Picometrix systems, it was shown during experimentation that the Picometrix system was able to penetrate both thicker and wetter samples than the Terasense system, and these results confirmed that the Picometrix system has overall stronger performance in terms of signal to noise ratio than the Terasense system, which is why more data is presented from the Picometrix system.

5.1.4 Predicting Dry Mass

The excellent linearity of the phase shift with mass allows for prediction of mass. To test how accurate this method is at predicting mass values using the phase shift measurements, the measured phase shift values of the samples are inputted into the best fit line equation of Figure 16 to calculate predicted mass values. The mass predicted in this way can then be compared to the actual mass values that were measured in the lab using a scale. This method produces a strong correlation between measured and predicted masses as would be expected,

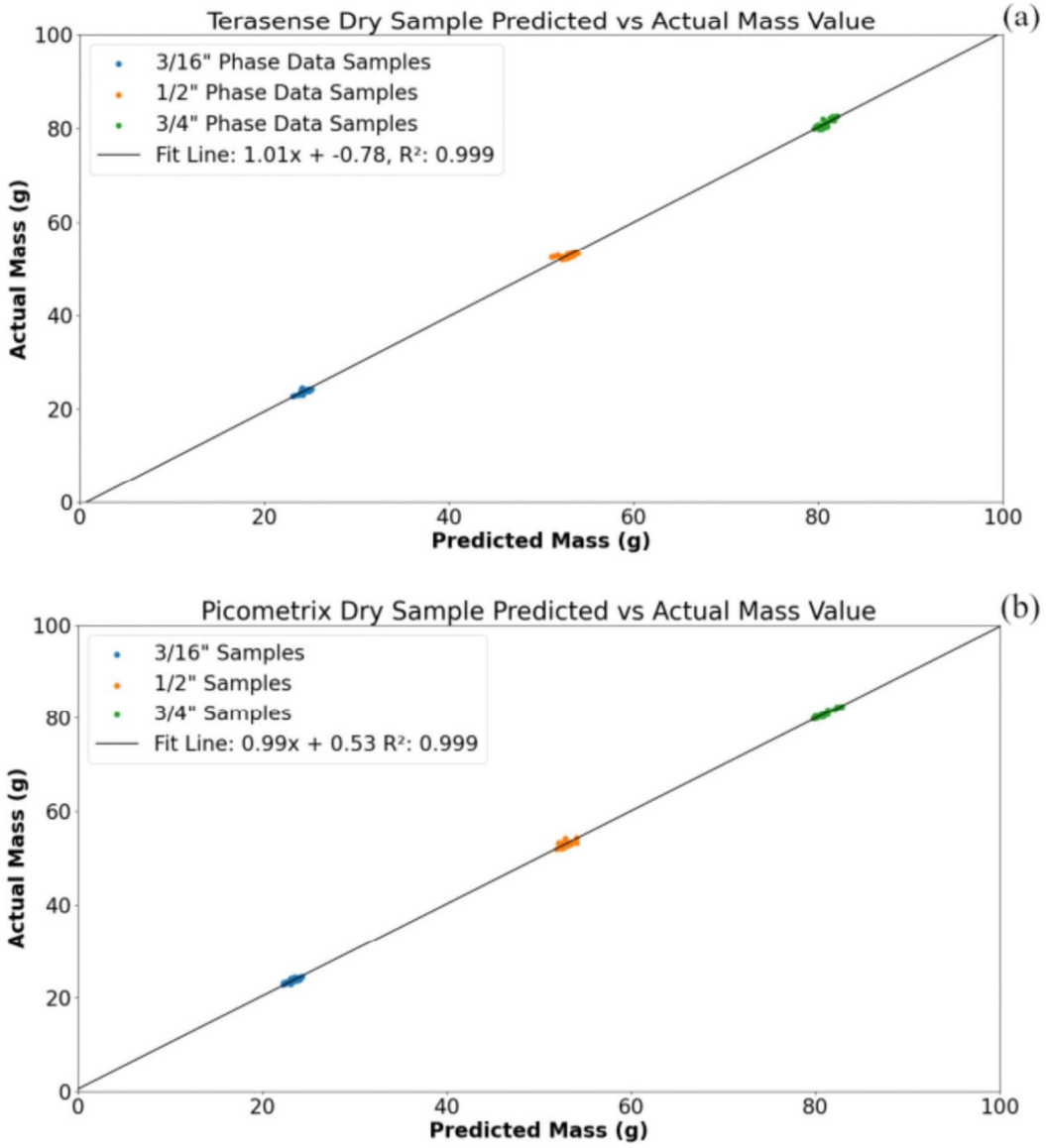

Figure 18: Mapping predicted mass values based on least squares regression fit from Figure 16 with actual measured mass shows strong predictive capability. Both Terasense and Picometrix system show minimal variance between predicted and actual mass

As we see in both Figures 18a and 18b, the predicted values line up well with their actual mass values. As shown in the graphs, both the Terasense and Picometrix results had R^2 values of 0.999.

5.2 Wet Sample Results

5.2.1 Expected Wet Results

The wet samples were prepared by organizing and placing the samples into the different conditioning environments of the desiccators as explained in Chapter 4.1, where they absorb water to different moisture content values. They were then measured in the same way as the dry samples as detailed in Chapter 4.3.1. Equation (22) will again determine the expected results but will now be dictated by the dielectric function of wet wood from equation (27) as opposed to the oven-dry function from equation (13). As such, we still expect to see a linear relationship as phase shift varies with mass and an exponential decay as amplitude varies with mass. However, the presence of the water is expected to make the results more pronounced as a THz signal will be affected by the water significantly more than the wood and resin in the samples due to the significantly higher absorption. This behaviour is reflected in equation (27), as the fractional composition of water f_w is a much larger contributor to the overall dielectric function in both the real and imaginary parts of the index compared to the fractional composition of the cell wall f_{cw}. We also expect to see similar linear and exponential relations as phase shift and amplitude are varied with moisture content, as the moisture content is directly proportional to f_w as seen in equation (30).

In summary, the expectations for the wet samples are:

- Measured phase still varies linearly with density/mass
- Measured relative amplitude still varies exponentially with density/mass
- Measured phase varies linearly with moisture content
- Measured relative amplitude varies exponentially with moisture content

5.2.2 Phase - Mass Results

As expected, the linear phase relation is maintained with the wet samples as shown in Figure 19.

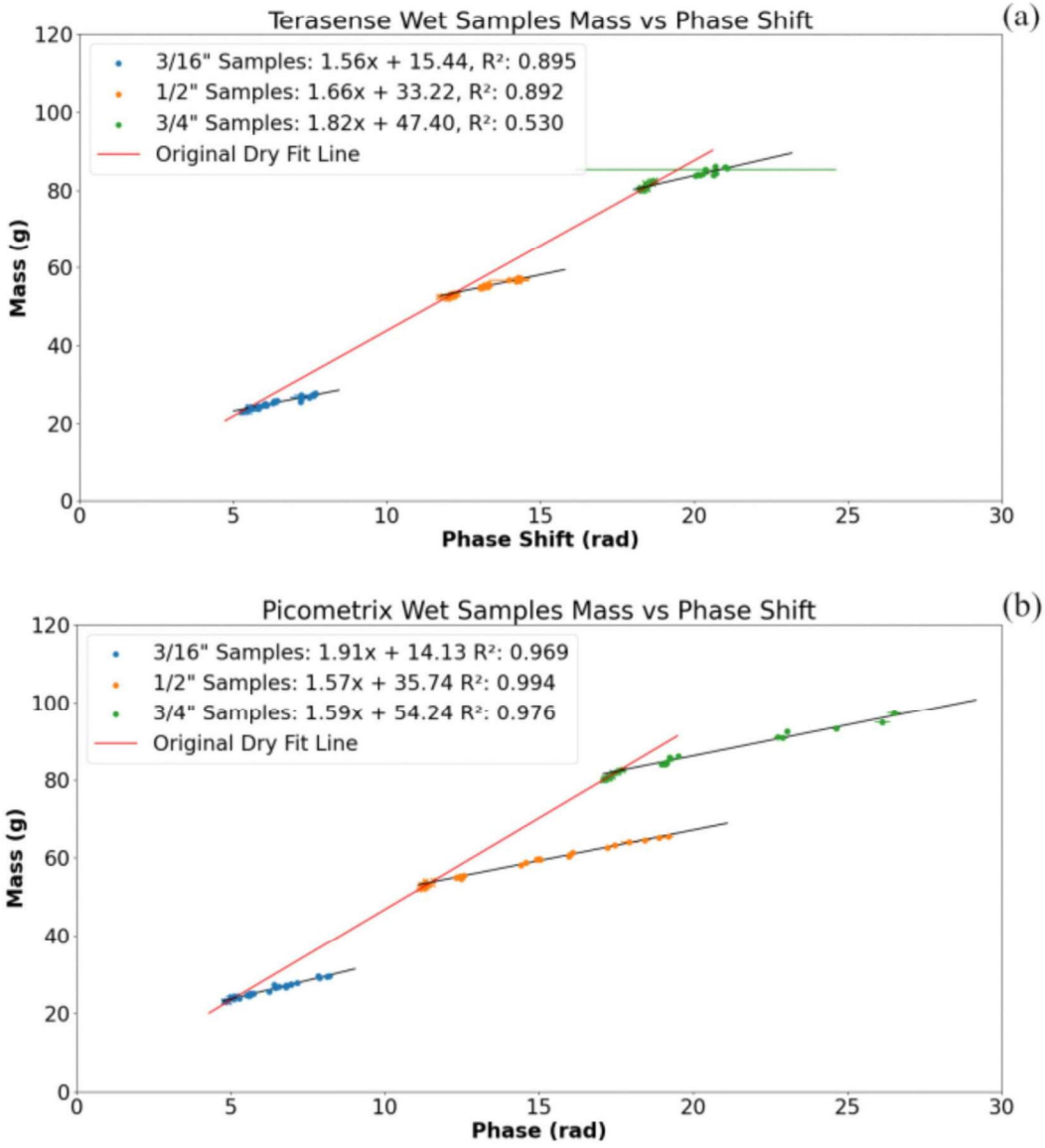

Figure 19: Mapping of wet sample mass to phase shift. Red line represents fit line from Figures 16a and 16b. Strong linear relation as was seen with dry samples but with stratified relations, while original dry data is inline with new linear relations. Terasense and Picometrix results similar with less variance in Picometrix due to higher sample count.

However, unlike with the dry samples, the relationship is stratified between thickness groupings. We can see this comparison directly with the red line in both Figures 19a and 19b as well as the "x" markers being the original fit and data points from Figures 16a and 16b. This is to be expected since, as an example, a 3/16" sample at 4% moisture content with the same length/width dimensions as a 1/2" sample at the same 4% moisture content will hold less water, since the difference between the thinner and thicker samples' sizes would intuitively mean that different amounts of water is needed to get to the same

4% moisture content. As well, the larger phase shift values compared to the dry samples confirms that water has a larger effect on phase shift as expected based on equation (27). This leads to a broader distribution of phase shift values. Even then, the dry sample data fits perfectly on the separate fit lines. As well, when comparing the slope of the lines in both Figures 19a and 19b we could make an assumption that the change in phase shift relative to change in mass is practically equivalent across samples, as most of the best fitting lines had a slope value roughly between $1.56 - 1.66 \frac{g}{rad}$.

5.2.3 Amplitude - Mass Results

In wet samples, the exponential decay is more prevalent, and the stronger signal of the Picometrix system provides cleaner data at higher moisture content.

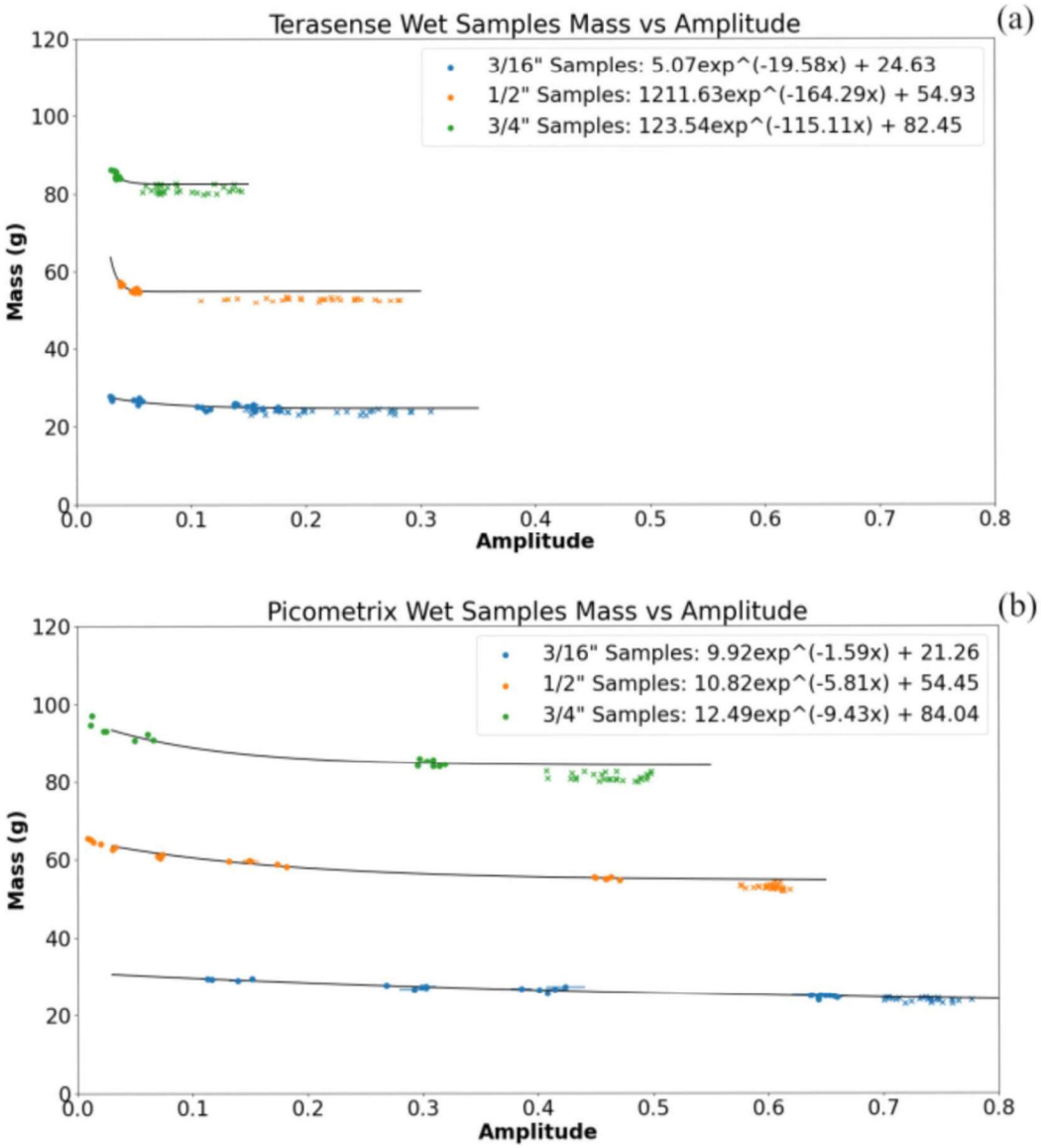

Figure 20: Mapping of wet mass to relative amplitude. Exponential results seen when compared to dry sample. Original dry results represented by "x" markers. Lower sample population in Terasense data set hinder results, but exponential relation is still evident

This is in line with our expectations from Chapter 5.1.1, and again shows that water has a much larger effect on the overall results, as we recover an exponential dependence of amplitude on mass within thickness groupings which was not evident in Chapter 5.1.3. In fact in the dry sample vs amplitude data from Figure 17, which is represented as the

"x" markers in Figure 20, we see it generally line up with the fitting equation generated by the wet data. Of note, there is a rough cut-off in the Terasense's amplitude value at approximately 0.03, which translates to 3% signal amplitude of the sample beam relative to the reference beam, as amplitude is dictated by the value of α from equation (8) in Chapter 4.3.1. This reinforces water's effect on signal, as the dryer and thinner samples still weakened the signal measured by the Terasense system significantly relative to the oven-dried results. However, the results from Terasense are hampered by the lack of samples caused by the lower signal amplitude measurement threshold, as the dry samples signal retention ranged between 5% and 30% and thus even an added reduction of just over 2% could render the sample immeasurable by the Terasense system. But when looking at Picometrix results, the exponential relation is much more evident. As well, when looking at the results of the Picometrix system we see that as the samples thickens, the amplitude and decay values of the fitting line increase as well, compared to the slopes from Chapter 5.2.2 which only varied slightly. Another thing of interest is the asymptotes of all the fitting lines are close to the average value of oven-dry sample masses relative to thickness, only off by about 2 to 3 grams. This is interesting since one would expect that at $\alpha = 1$, the results would be equivalent to the reference arm of the sample with no sample, ie no mass to measure.

5.2.4 Predicted Wet Mass

Given the strong relation of both the phase shift and amplitude with the mass, we can use the least squares fitting equations from Figures 19 and 20 to predict the mass values of the samples and compare them to the actual mass as we did in Section 5.1.4. Here the mass is predicted by either taking the measured phase shift or amplitude and using the appropriate least squares fitting equation matching the sample's thickness group. For example, if we take the measured phase shift of a sample we would then input it into the least fit square equation appropriate to its thickness from Figure 19, ie if the sample was in the 1/2" thickness group and the phase shift value came from the Terasense system, then the value would be replace x in the equation $y = 1.66x + 33.22$ from Figure 19a and y would be the resultant predicted mass. Similarly for the measured amplitude and the appropriate equation from Figure 20. As such, there are 2 predicted mass values for each sample: one based on its phase shift and one based on its amplitude. Again, actual mass values are the wet masses of the samples when measured by a scale.

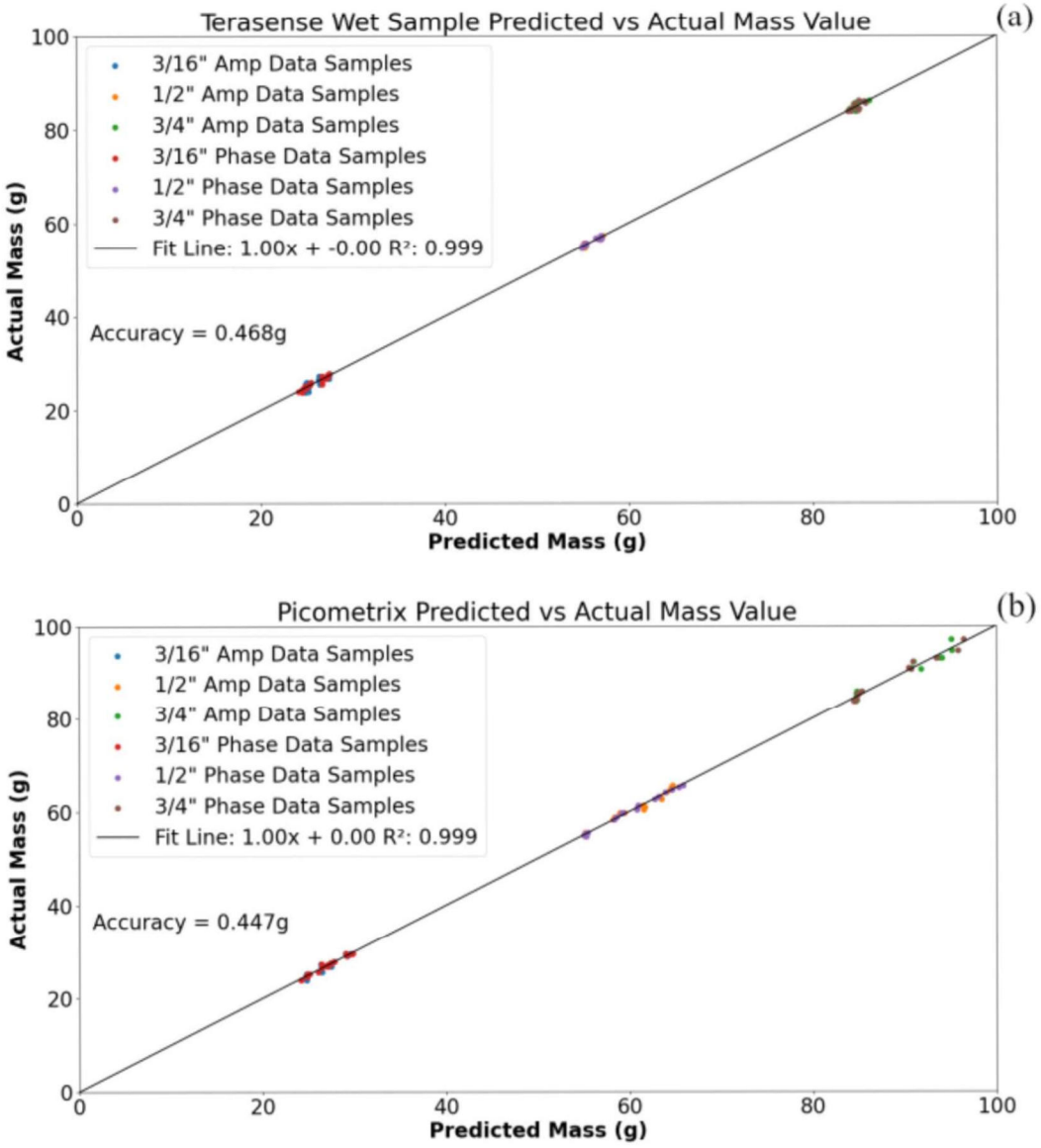

Figure 21: Mapping of measured wet mass to wet mass predicted by fitting equations from Figures 19 and 20. Wet mass prediction near perfect when using least squares fitting of linear phase relation and exponential amplitude relation

Here we see a strong potential for mass prediction, with only a slightly higher variance in the Picometrix system compared to the Terasense system, likely resulting from the larger number of samples to compare. Accuracy was found to be within just under $0.5g$, which equates to roughly 1-2% uncertainty in the mass. The accuracy was calculated using the average of the RMSE between the actual and predicted values as was done in the UHMW tests and will be done for the rest of the accuracy predictions.

5.2.5 Phase Shift - Moisture Content Results

As was predicted in 5.2.1, we see a strong linear relationship as moisture content is varied with phase shift.

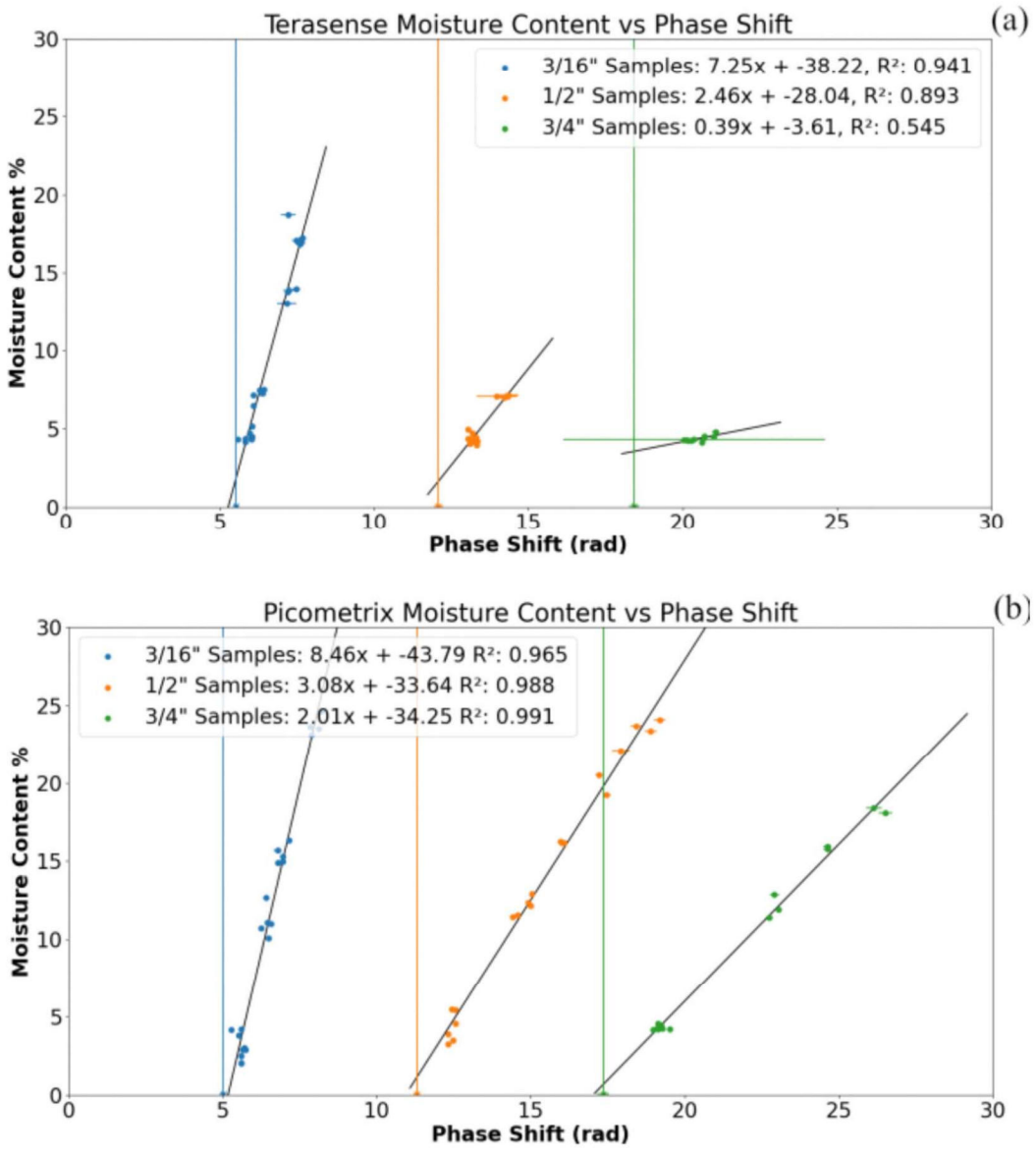

Figure 22: Mapping of moisture content to phase change. Linear relation between moisture content and phase shift is confirmed. X-intercept also shown to be close to average phase shift value of dry samples as represented by vertical lines

As expected, the lower sample numbers measured with the Terasense system reduces the accuracy of the fitting line, but results still show a strong correlation to what was expected from Chapter 5.2.1. Of note is the change in slope between thickness groups. This is to be expected, as it follows from what was intuited in Chapter 5.2.2, where thinner

samples will need less water to reach the same moisture content as thicker samples, and because more water will have an overall higher effect on the phase shift a larger change in phase shift is expected across the same change in moisture content relative to thickness. Also of note is the x-intercept of most of the fitting lines are approximately equal to the average of the phase shift for the dry samples. The only exception to this is $3/4$" samples measured with the Terasense system, which can be expected with it being the group with the lowest number of samples. This shows that the results are in line with one another.

5.2.6 Amplitude - Moisture Content Results

We see a similar exponential relationship between moisture content and amplitude as we did in Chapter 5.2.3.

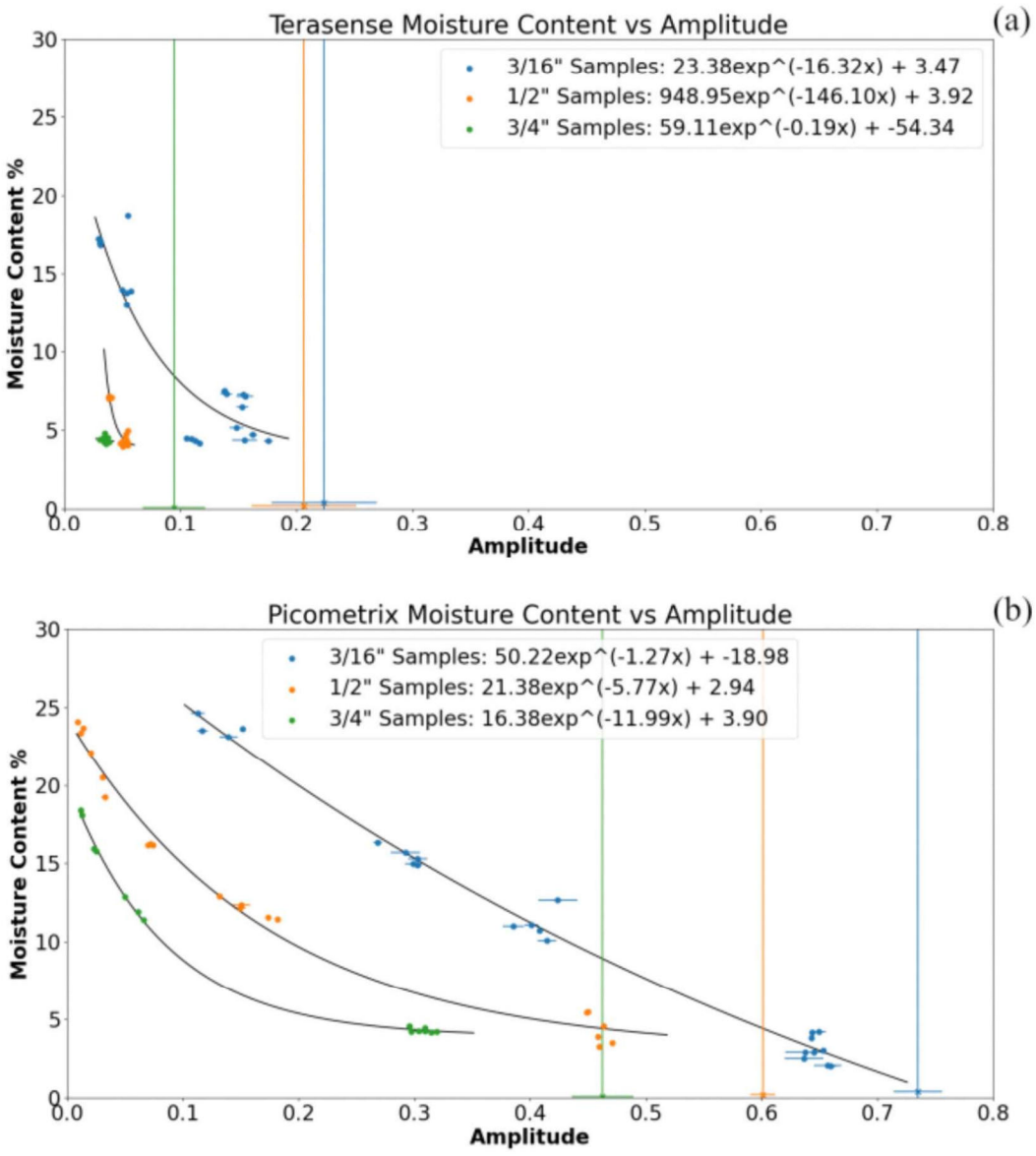

Figure 23: Mapping of moisture content to relative amplitude. Exponential relation seen when varying moisture content with amplitude, especially in Picometrix data set

Again the relation is more pronounced in the Picometrix system due to the higher signal retention. Again the average of the amplitude value is close to fitting with a potential x-intercept, but the higher variance in the dry amplitude values from Figure 17 increased the standard deviation of the mean. These results are again in line with what was expected from equations (22), (27) and (30). Since the thicker samples needed to

retain higher volumes of water to meet the same moisture content as thinner samples, the effect moisture content has upon the signal is greater.

5.2.7 Predicted Moisture Content Results

As was done before in Sections 5.1.4 and 5.2.4 we can use the least-squares fit equations of Figures 22 and 23 to compare a predicted moisture content value to the known moisture content value for both the Terasense and Picometrix systems. Again, as with Section 5.2.4, each sample will have 2 predicted moisture contents: one based on its phase shift and the other based on its amplitude. To acquire an actual moisture content value the standard equation for measuring moisture content is used,

$$MC = \frac{\rho_{od} - \rho_{ww}}{\rho_{od}} \tag{35}$$

where ρ_{ww} is the wetwood density and ρ_{od} is the oven-dry density. Using the measured versions of the densities based on their volumetric values we get actual moisture content values for comparison.

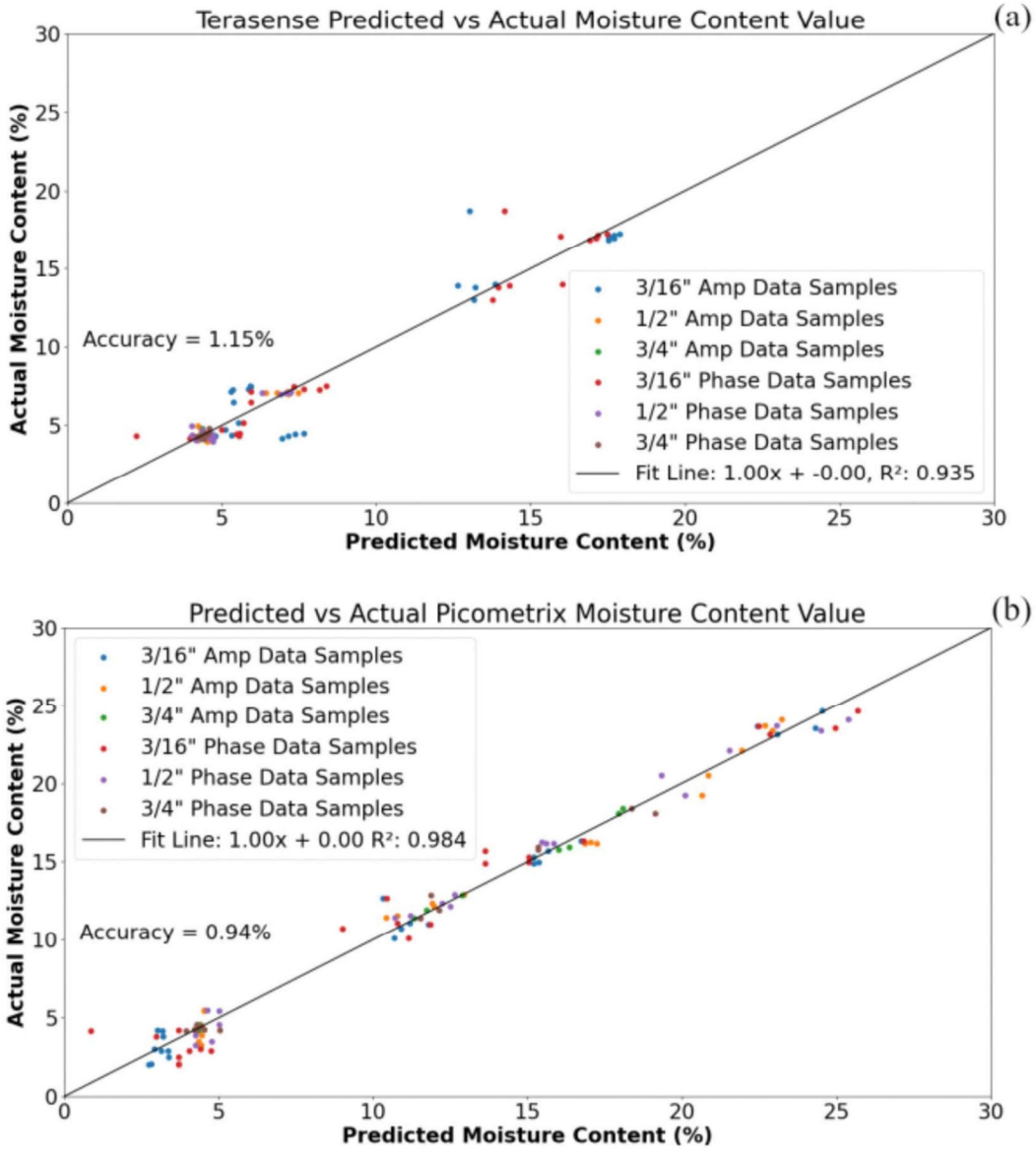

Figure 24: Mapping of measured moisture content to moisture content predicted by fitting equations from Figures 22 and 23. While less accurate then prediction of wet mass values, prediction of moisture content still highly accurate. Picometrix's higher signal strength allowed for more accurate results, but Terasense was still decently accurate.

Compared to the mass predictions, the moisture content predictions are less accurate, but the results are still reasonable, with an R^2 value of 0.935 and 0.984 for the Terasense and Picometrix systems respectively. Most important is the 1.15% and 0.94% accuracy of the Terasense and Picometrix systems respectively, again based on the average for the RMSE of the predictions. These results for MDF need to be within 2-3% to be considered accurate[European Panel Federation, 2015], therefore we can say that prediction of moisture content using phase shift and amplitude more than meets industry standards.

Therefore, since we can accurately predict the moisture content of the samples we will see if the same can be said for the prediction of density.

5.3 Simultaneous Prediction of Dry Density and Moisture Content

As shown with the previous graphs, relations between the phase shift and amplitude with the mass and moisture content can be easily seen. But the most important thing is to determine if by combining these relations we can simultaneously predict both the dry density and moisture content of a sample using the phase shift and amplitude data. Chapter 5.2.7 has already shown that we can accurately predict the moisture content, but the oven-dry density will require a bit more work. For this we use the least-squares fitting line equations from Figures 19 and 23 and the relation between the density and moisture content to calculate a predicted dry density to compare to the actual measured dry density. The relation between moisture content and density is defined by equation (35), and can be rewritten as,

$$\rho_{od} = \frac{\rho_{ww}}{\frac{MC}{100\%} + 1} \tag{36}$$

First we begin by calculating a predicted moisture content using the amplitude, as was done in Section 5.2.7, since the phase shift has a stronger physical correlation with changes in mass than moisture content. Then, the wetwood density is calculated by predicting the wet mass as was done in Section 5.2.4 given the measured phase shift then dividing it by an arbitrary volume value based on the sample's thickness group and the standard 75 mm x 75 mm surface area of the samples. For example the 1/2" samples would have an arbitrary volume of 71.4 cm^3. Combining both values with (36) will give an oven-dry density we can compare with the known oven-dry density. As such, using the data from both the Terasense system and the Picometrix system two graphs where created to compare the predicted density from (36) with the actual measured density,

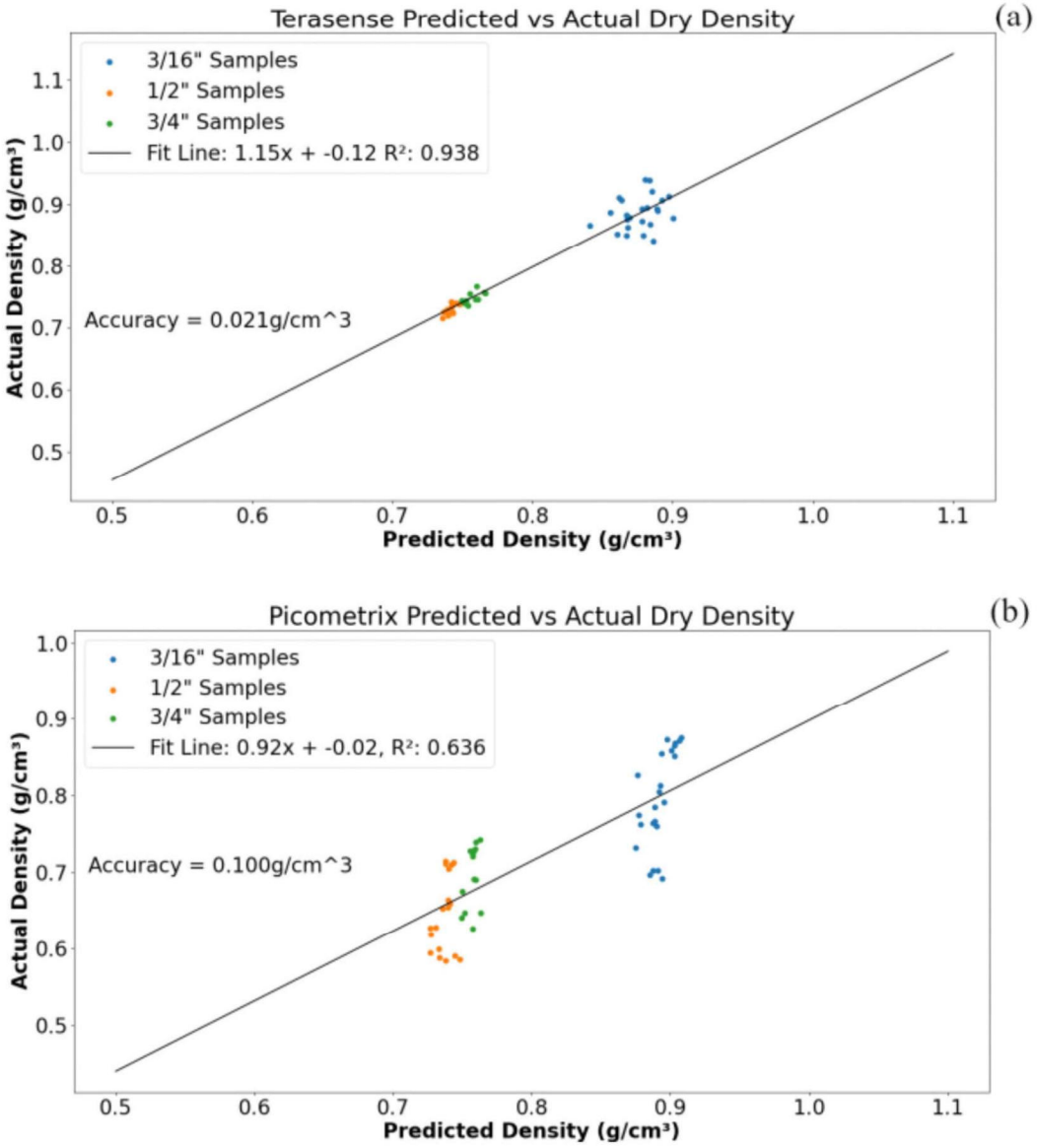

Figure 25: Mapping of measured density to predicted density. Terasense system shows fairly accurate prediction, with actual results skewing slightly higher than predicted. However an unknown factor skewed Picometrix predictions.

As we can see in Figure 25, the Terasense system is very good at predicting the dry density value, yielding a fitting line with an R^2 of 0.938. As well, it has an excellent accuracy of $0.021 g/cm^3$, consistent with the variation commonly seen in commercial grade MDF[Theng et al., 2015]. Again, accuracy was measured as the average of the RSME of the predictions to the actual density. Meanwhile, the Picometrix system gives a lower R^2 of 0.636 for dry density measurements. The shape of the data relative to thickness suggests an unknown factor in the Picometrix data that was unaccounted for. Still, this shows that simultaneous prediction of dry density and moisture content using

only the phase shift and amplitude values of a THz spectroscopy system is possible.

6 Conclusions and Future Work

As shown by the results of Chapter 5.3, the simultaneous prediction of dry density and moisture content of wood given the measured phase shift and amplitude values of a THz spectroscopy system is possible. Given that the samples were chosen for their arbitrary randomness in composition and still were able to be properly measured while using a simpler EMT than used by more uniform, heterogeneous materials shows that this method will work for those materials as well. This means that other methods capable of measuring the phase shift and amplitude that can be scaled for a full sheet of MDF or other large wood product are viable technology to replace older methods that heavily relied on product destruction. The results to bring up a few unanswered questions though, since considering the prevalence of UF resin in many wood products like MDF, it would be best to determine the properties of resin in a THz spectroscopy system. This will help determine the cause behind the high variance in the amplitude data of the dry samples in Chapter 5.1.3, whether it is the resin or some other avenue of investigation.

To continue this work, it is important to refine our knowledge of the materials used in the experiment. As mentioned in Chapter 5.1.3, MDF is made of not just wood chips of various species but resin as well. The amount of resin in MDF could be significant enough to effect the dielectric function of both the oven-dry samples and wet-wood samples, but to determine the complex values of it's dielectric function was outside the scope of this experiment. However, if one were to take UF resin and compress them into pucks of solid resin, they could be measured using a THz spectroscopy system like the Picometrix system to determine their dielectric function. As well, this experiment could be broadened by using different sample types such as plain hardwood and softwood, or other composite materials such as plywood or low-density fiberboard, ie particle board. While the system was sufficiently accurate for MDF, it could be possible that it is less so for pure wood samples, especially wood with a higher surface roughness to affect the beam. As well, it would be pertinent to determine if higher frequency THz systems would improve the accuracy. But most importantly the odd results of the Picometrix systems prediction needs to be investigated as well, so that the unknown factor skewing the results can be determined. In the end, the simultaneous prediction of density and moisture content in the wood industry provides a useful application for THz spectroscopy technology.

References

[Bal and Gündeş, 2020] Bal, B. C. and Gündeş, Z. (2020). Surface roughness of medium-density fiberboard processed with cnc machine. *Measurement*, 153:107421.

[Banerjee et al., 2008] Banerjee, D., von Spiegel, W., Thomson, M. D., Schabel, S., and Roskos, H. G. (2008). Diagnosing water content in paper by terahertz radiation. *Opt. Express*, 16(12):9060–9066.

[Bogosanovich et al., 2009] Bogosanovich, M., Al Anbuky, A., and Emms, G. (2009). Microwave measurement of wood in principal directions. In *SENSORS, 2009 IEEE*, pages 252–256.

[Domínguez-Robles et al., 2020] Domínguez-Robles, J., Tarrés, Q., Alcalà, M., El Mansouri, N.-E., Rodríguez, A., Mutjé, P., and Delgado-Aguilar, M. (2020). Development of high-performance binderless fiberboards from wheat straw residue. *Construction and Building Materials*, 232:117247.

[Eroğlu et al., 2001] Eroğlu, H., İstek, A., and Usta, M. (2001). Medium density fiberboard (mdf) manufacturing from wheat straw (triticum aestivum l.) and straw wood mixture.

[European Panel Federation, 2015] European Panel Federation (2015). Controlling MDF Moisture Content. https://mdf-info.eu/using-mdf/handling-and-storing/controlling-moisture-content.

[Federici, 2012] Federici, J. F. (2012). Review of Moisture and Liquid Detection and Mapping using Terahertz Imaging. *Journal of Infrared, Millimeter, and Terahertz Waves*, 33(2):97–126.

[Gehloff et al., 2020] Gehloff, M., Reid, M., Hartley, I. D., Price, B., and Mucchi, L. (2020). Density scanner for engineered wood products using a realtime sub-thz imaging camera. In *Imaging and Applied Optics Congress*, page ITu4G.2. Optica Publishing Group.

[Hadjiloucas et al., 1999] Hadjiloucas, S., Karatzas, L., and Bowen, J. (1999). Measurements of leaf water content using terahertz radiation. *IEEE Transactions on Microwave Theory and Techniques*, 47(2):142–149.

[Hashin, 1983] Hashin, Z. (1983). Analysis of Composite Materials—A Survey. *Journal of Applied Mechanics*, 50(3):481–505.

[Inagaki et al., 2014] Inagaki, T., Ahmed, B., Hartley, I. D., Tsuchikawa, S., and Reid, M. (2014). Simultaneous prediction of density and moisture content of wood by terahertz time domain spectroscopy. *Journal of Infrared, Millimeter, and Terahertz Waves*, 35(11):949–961.

[Jepsen et al., 2007] Jepsen, P. U., Møller, U., and Merbold, H. (2007). Investigation of aqueous alcohol and sugar solutions with reflection terahertz time-domain spectroscopy. *Opt. Express*, 15(22):14717–14737.

[Jördens et al., 2010] Jördens, C., Wietzke, S., Scheller, M., and Koch, M. (2010). Investigation of the water absorption in polyamide and wood plastic composite by terahertz time-domain spectroscopy. *Polymer Testing*, 29(2):209–215.

[Mousavi et al., 2009] Mousavi, P., Haran, F., Jez, D., Santosa, F., and Dodge, J. S. (2009). Simultaneous composition and thickness measurement of paper using terahertz time-domain spectroscopy. *Applied Optics*, 48(33):6541.

[Oshina and Spigulis, 2021] Oshina, I. and Spigulis, J. (2021). Beer–Lambert law for optical tissue diagnostics: current state of the art and the main limitations. *Journal of Biomedical Optics*, 26(10):100901.

[Phanopolus, 2010] Phanopolus, C. (2010). *Polyurethanes and Isocyanates used as adhesives in Composite Wood Products*.

[Price et al., 2020] Price, B. D., Lowry, S. N., Hartley, I. D., and Reid, M. (2020). Sub-terahertz refractive flat-top beam shaping via 3d printed aspheric lens combination. *Applied Optics*, 59(18):5429–5436.

[Reid et al., 2013] Reid, M., Hartley, I., and Todoruk, T. (2013). *Handbook of terahertz technology for imaging, sensing and communications*, chapter 19, pages 547–574. Elsevier.

[Theng et al., 2015] Theng, D., Arbat, G., Delgado-Aguilar, M., Vilaseca, F., Ngo, B., and Mutjé, P. (2015). All-lignocellulosic fiberboard from corn biomass and cellulose nanofibers. *Industrial Crops and Products*, 76:166–173.

[Wang et al., 2019] Wang, H., Inagaki, T., Hartley, I. D., Tsuchikawa, S., and Reid, M. (2019). Determination of Dielectric Function of Water in THz Region in Wood Cell Wall Result in an Accurate Prediction of Moisture Content. *Journal of Infrared, Millimeter, and Terahertz Waves*, 40(6):673–687.

[Wilson, 2008] Wilson, J. B. (2008). Medium density fiberboard (mdf): A life-cycle inventory of manufacturing panels from resource through product. *Final Report to the Consortium for Research on Renewable Industrial Materials*.

[Yang and Huang, 2007] Yang, W. Z. and Huang, J. P. (2007). Effective mass density of liquid composites: Experiment and theory. *Journal of Applied Physics*, 101(6):064903.

[Zhang et al., 2018] Zhang, H., Li, Z., Chen, T., and Liu, J.-J. (2018). Detection of Poisonous Herbs by Terahertz Time-Domain Spectroscopy. *Journal of Applied Spectroscopy*, 85(1):197–202.

[Zhang et al., 2015] Zhang, N., Li, S., Xiong, L., Hong, Y., and Chen, Y. (2015). Cellulose-hemicellulose interaction in wood secondary cell-wall. *Modelling and Simulation in Materials Science and Engineering*, 23(8):085010.